Chapter 5

Fluorescence of Molecules near Anisotropic Gold Nanostructures

Fluorescence of Molecules near Anisotropic Gold Nanostructures

Metallic particles at the nanoscale dimension tend to afford spherical geometry to reduce surface free energy. However, under restricted condition, the emergence of novel properties of these anisotropic structures could be attributed to the lack of symmetry at the interface or to the confinement of electrons that does not scale linearly with size. The anisotropicity of the nanostructures may start from the ellipsoids and gradually become complex with star-shaped structures. In this chapter, we have selected dog-bone shaped nanorods and nanospikes of gold to study the emission behavior of fluoroprobes near these intricate nanostructures. This chapter contains two sub-sections:

5.1. Aspect Ratio Dependence of Dogbone-Shaped Gold Nanorods

5.1.1. Introduction

Studies on the interaction of organic fluorophores with noble metal nanostructures have stimulated research both in basic science and technology.[1-3] Metallic particles *viz.*, copper, silver and gold, in the nanometer size regime exhibit strong absorption in the visible region, often coined as localized surface plasmon resonance (LSPR).[4] The resonance frequency of this LSPR is strongly dependent upon the size, shape, interparticle interactions, dielectric properties, and local environment of the nanoparticles.[5] Apart from spherical nanoparticles, many anisotropic structures of noble metal nanoparticles with excellent surface plasmon tunability and chemical stability have encouraged their applications in a diverse range of niche applications.[6] Gold nanorods have been demonstrated to be a highly promising class of plasmonic nanostructures as these particles exhibit transverse and longitudinal plasmon resonances that correspond to electron oscillations perpendicular and parallel to the rod length direction, respectively.[7] Organic fluoroprobes have often been used as local probes for the physicochemical characterization of the nanostructures and the resultant organic-inorganic hybrid nanoassemblies could be utilized for the development of plasmonic nanoemitters.[8, 9]

Recently, gold nanorods have been used to modify intrinsic fluorescence of molecular probes theoretically and experimentally by adjusting the nanorod size and its aspect ratio.[10, 11] To date, studies on the interaction of fluorophores with the gold nanorods have predominantly focused on the fluorescence intensity enhancement in the metal-fluoroprobe hybrid nanoassemblies. Halas and colleagues have studied the fluorescence enhancement of the near-infrared fluorophore IR800 by gold nanorods and it was revealed that the quantum yield of IR800 is enhanced ten-fold on the surface of the nanorods.[12] Wang and group have demonstrated direct measurement of the plasmonic-molecular resonance coupling as a function of the nanorod plasmon resonance wavelength.[13] Fu et al. observed a remarkable increase in the fluorescence of a single fluorophore controllably linked to ends of a single gold nanorod.[14] Gong and co-authors have employed FDTD method to investigate single-molecule spontaneous emission that reveals gold nanorod antenna can maintain large field enhancement within the nanorod's longitudinal plasmon resonance band while the emission behavior around the nanorod's short-axis resonance band is similar to that of a spherical particle.[15] Ming et al. reported the strong polarization dependence of the plasmon-enhanced fluorescence where the fluorophores were embedded in a silica shell around an individual gold nanorod.[16] Singamaneni and colleagues have investigated the influence of gold nanorod dimensions on distance-dependent LSPR sensitivity and electromagnetic decay length using electrostatic layer-by-layer assembly of polyelectrolytes and developed plasmonic nanotransducers for label-free biological sensing.[17] Lu et al. have designed a fluorescence resonance energy transfer system containing gold nanorods and fluorescein for the detection of hepatitis B virus DNA sequences.[18]

In this Sub-section, we have investigated the aspect ratio (length-to-diameter ratio; l/d) dependence of the 'dogbone-shaped gold nanorods' (GDNRs) on the emission behavior of sudan red 7B molecules. Although the fundamental physics of the processes involved is well-known, the effects of several parameters have remained unaddressed in the literature. It is seen that the probe molecules adsorbed onto the surface of GDNRs exhibit strong quenching of their fluorescence and the extent of quenching differs with different aspect ratio of the nanorods. The quenching efficiency in the presence of variable aspect ratio of the rods has been attributed to the surface area dependence arising

as a result of cumulative effect of the length and diameter of the nanorods. The mechanism of quenching has been enlightened in the view of electron and energy transfer processes in the metal-fluoroprobe hybrid nanostructures.

5.1.2. Experimental Section

5.1.2.1. Synthesis of Gold Dogbones of Variable Aspect Ratio

Gold dogbones have been synthesized by seed-mediated growth process by following the protocol of Gou et al.[19] In this method, the aspect ratio of the GDNRs has been varied using the different concentration of $AgNO_3$ solution into the reaction mixture. The synthesis of GDNRs has been accomplished in two main steps:

5.1.2.1.1. Preparation of Gold Seeds

Aqueous dispersion of gold seed was prepared by mixing solutions of $HAuCl_4.3H_2O$ (5 mL, 0.5 mM) and CTAB (5 mL, 0.2 M) under stirring, which forms deep yellow color. Then, an aliquot of freshly prepared ice-cold $NaBH_4$ solution (0.6 mL, 10 mM) was added instantaneously into the reaction mixture and stirring was continued for 10 mins. The color of the solution changes to deep brown indicating the formation of gold seed and the dispersion was aged, further, for 3-4 h prior to the synthesis of GDNRs.

5.1.2.1.2. Preparation of Gold Dogbones

The growth solution for the synthesis of dogbones (adding on to the ends of the nanorods) consists of $HAuCl_4.3H_2O$ (5 mL, 1 mM), CTAB (5 mL, 0.2 M) and $AgNO_3$ (4 mM of volume varying from 80 to 300 µL) and freshly prepared ascorbic acid (70 µL, 0.1 M) solution were added to the above mixture, just to make the solution colorless. Then, 10 µL of the dispersion of gold seed was added, mixed by gentle shaking for one second and were kept undisturbed. The red to pink coloration was appeared slowly within 15 -20 mins indicating the formation of the rods. The synthetic conditions for the preparation of GDNRs with variable aspect ratio are shown in Table 5.1.

5.1.2.2. Preparation of Nanorod-Probe Hybrid Assembly

In a typical set, an aliquot of GDNRs (20 µM) from different sets was added to a solution of SR7B (0.3 µM) and the final volume of the solution was maintained to 5 mL. The solution was allowed to stand for 12 h to complete the surface complexation process and fluorescence of each solution was measured in the spectrofluorimeter.

Table 5.1. Composition of the Growth Solutions for the Synthesis of 'Dogbone-Shaped' Gold Nanorods

Set	Vol. of Au seed (0.25 mM) (μL)	Vol. of $HAuCl_4$ (1.0 mM) (mL)	Vol. of CTAB (0.2 M) (mL)	Vol. of $AgNO_3$ (4.0 mM) (μL)	Vol. of ascorbic acid (0.1 M) (μL)	λ_{max} at LSPW (nm)	Aspect ratio
SP	-	-	-	-	-	-	1.0±0.2
DNR1	10	5	5	80	70	613	1.7±0.3
DNR2	10	5	5	120	70	635	2.5±0.4
DNR3	10	5	5	140	70	651	3.2±0.5
DNR4	10	5	5	180	70	677	4.0±0.5
DNR5	10	5	5	220	70	700	4.8±0.5
DNR6	10	5	5	240	70	714	5.5±0.6
DNR7	10	5	5	300	70	748	6.0±0.7

5.1.3. Results and Discussion

Sudan Red 7B [N-ethyl-1-(4-phenylazo)phenylazo-2-naphthylamine] (extinction co-efficient 6200 $M^{-1}cm^{-1}$, quantum yield, $\varphi_f \sim 0.01$), also called 'oil violet', is a lipid staining dye of the member of Sudan family and is widely used for different scientific and industrial applications.[20] Figure 5.1 shows an absorption (0.16 mM) and emission (0.3 μM) profile of SR7B in aqueous solution. It shows a major absorption peak at 535 nm and a vibrational shoulder at 368 nm which might be attributed to the $\pi \rightarrow \pi^*$ and $n \rightarrow \pi^*$ transitions, respectively, corresponding to the monomeric form of the dye.[21] Excitation at 535 nm produces the emission spectrum with maximum at 619 nm. The molecular structure of SR7B is shown in the inset. We have studied the emission spectra of SR7B as a function of dye concentration in the range of 0.1 - 1 μM (not shown). It is found that there is no significant perturbation in the band structure and band position of the dye and fluorescence intensity (at 619 nm) increases linearly with increase in the concentration of the dye molecules indicating there is no significant dimerization or higher order aggregation in the prescribed concentration range. These characteristics have

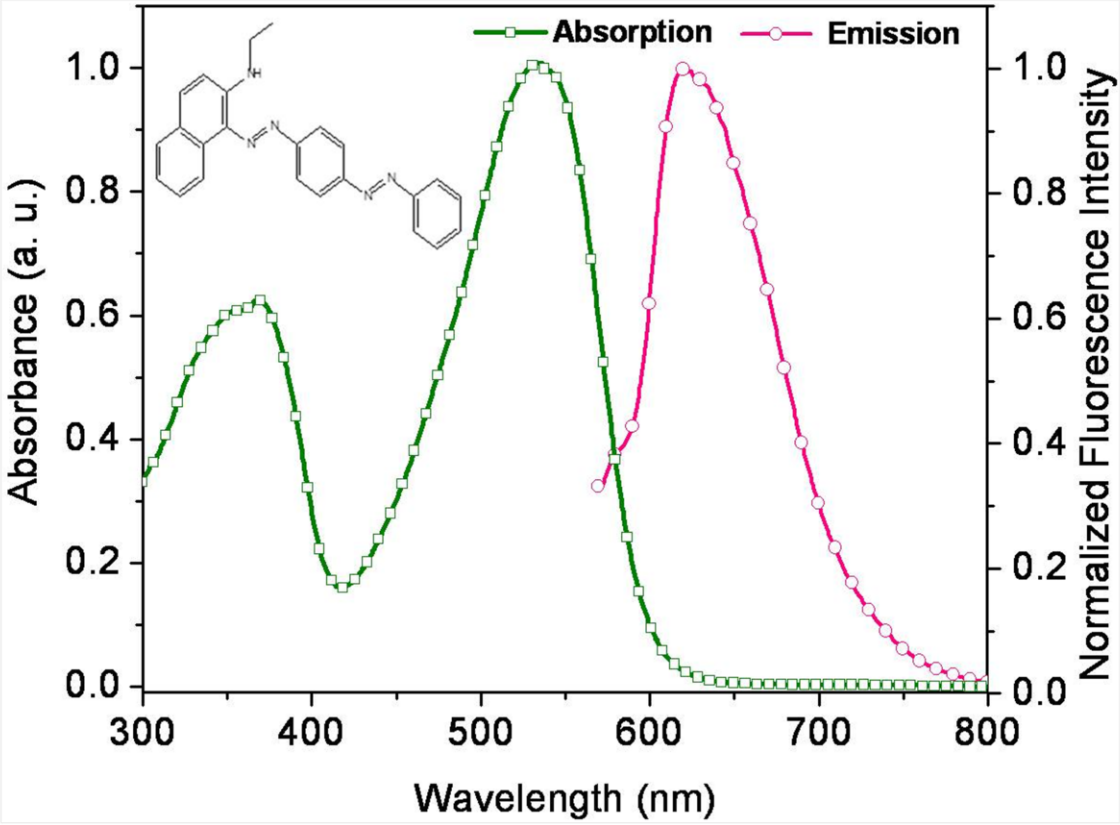

Figure 5.1. Normalized absorption and emission spectrum of Sudan Red 7B in aqueous solution. Molecular structure of the dye is shown in the inset.

enabled us to study the emission properties of the SR7B molecules with metallic nanostructures.

Gold nanorods with hemispherical caps looking 'dogbone-like' structures stabilized by cetyltrimethylammonium bromide were grown in aqueous solution using seed-mediated growth method.[19] Figure 5.2 shows the absorption spectra (0.25 mM) of spherical gold nanoparticles (SP) and GDNRs of variable aspect ratio. Inset shows TEM images of the end and side views corresponding to transverse and longitudinal plasmon resonances of the dogbones, which can be understood within the framework of Gans theory that describes the optical properties of ellipsoid nanoparticles based on dipole approximation.[22] The absorption spectra of the GDNRs exhibit two distinct maxima, a transverse plasmon band arising at around 530 nm that is associated with electron oscillation perpendicular to the length axis of the rods[7] and a longitudinal plasmon band (at >600 nm) that is associated with electron oscillations parallel to the rod length axis.[23]

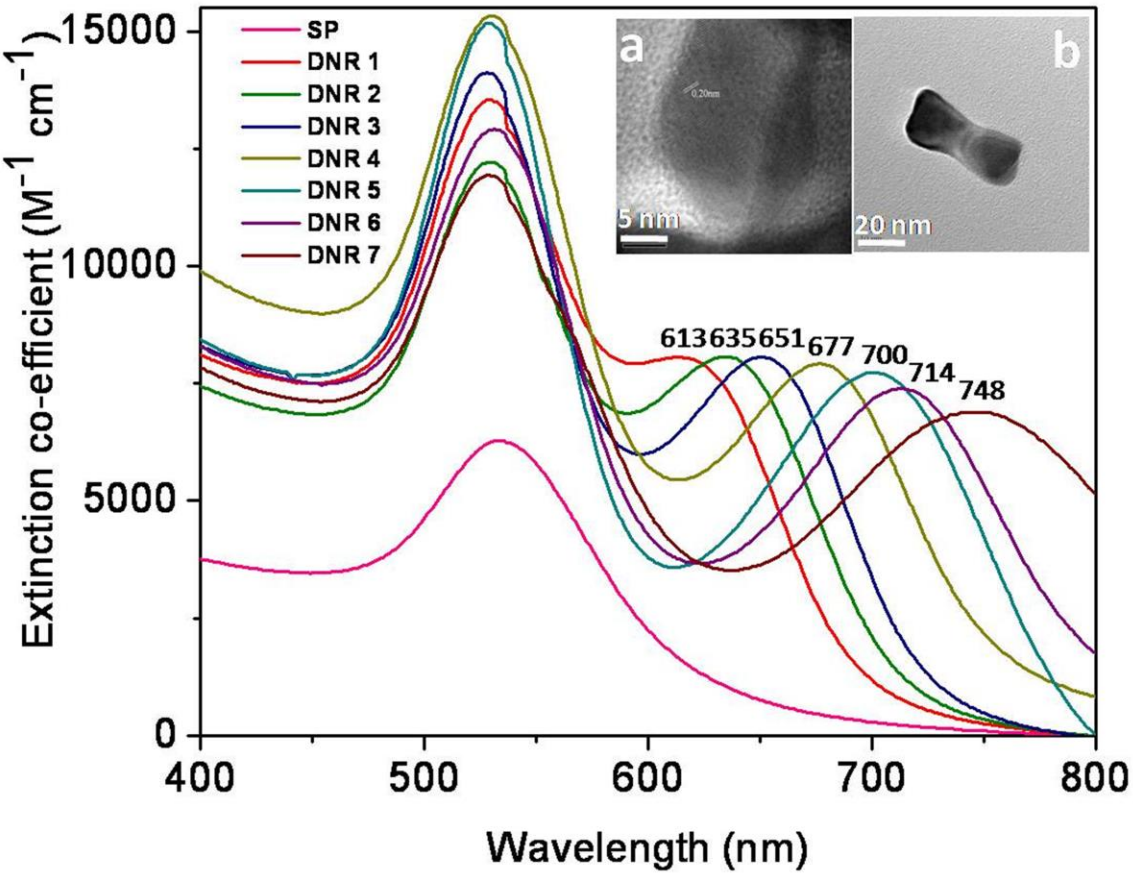

Figure 5.2. Absorption spectra of gold dogbones (0.25 mM) of variable aspect ratio. Inset shows TEM images of the (a) end and (b) side view corresponding to transverse and longitudinal plasmon resonances of the dogbones.

It is seen that the transverse surface plasmon is not influenced much by the aspect ratio of GDNRs, but longitudinal surface plasmons are highly sensitive and could be tuned from visible to the infrared regions by rational control over their aspect ratio.

Transmission electron micrographs of the representative GDNRs of sets SP, DNR 1, DNR 3 and DNR 6 are shown in Figure 5.3. It is seen that the nanorods having fatter ends and thinner middle sections are nearly monodisperse and the aspect ratio varies from 1 to 6 (for simplification, the nanospheres are treated as nanorods with aspect ratio 1). The average diameter for the spherical particles is 3-4 nm; average length and diameter of the dogbones are 20±10, 30±10 and 55±10 nm for DNR 1, DNR 3 and DNR 6 respectively. Gou et al. have pointed out that when the unpurified gold nanorods are treated with ascorbic acid, the nanorods act as seeds and subsequently, reduced gold atoms were

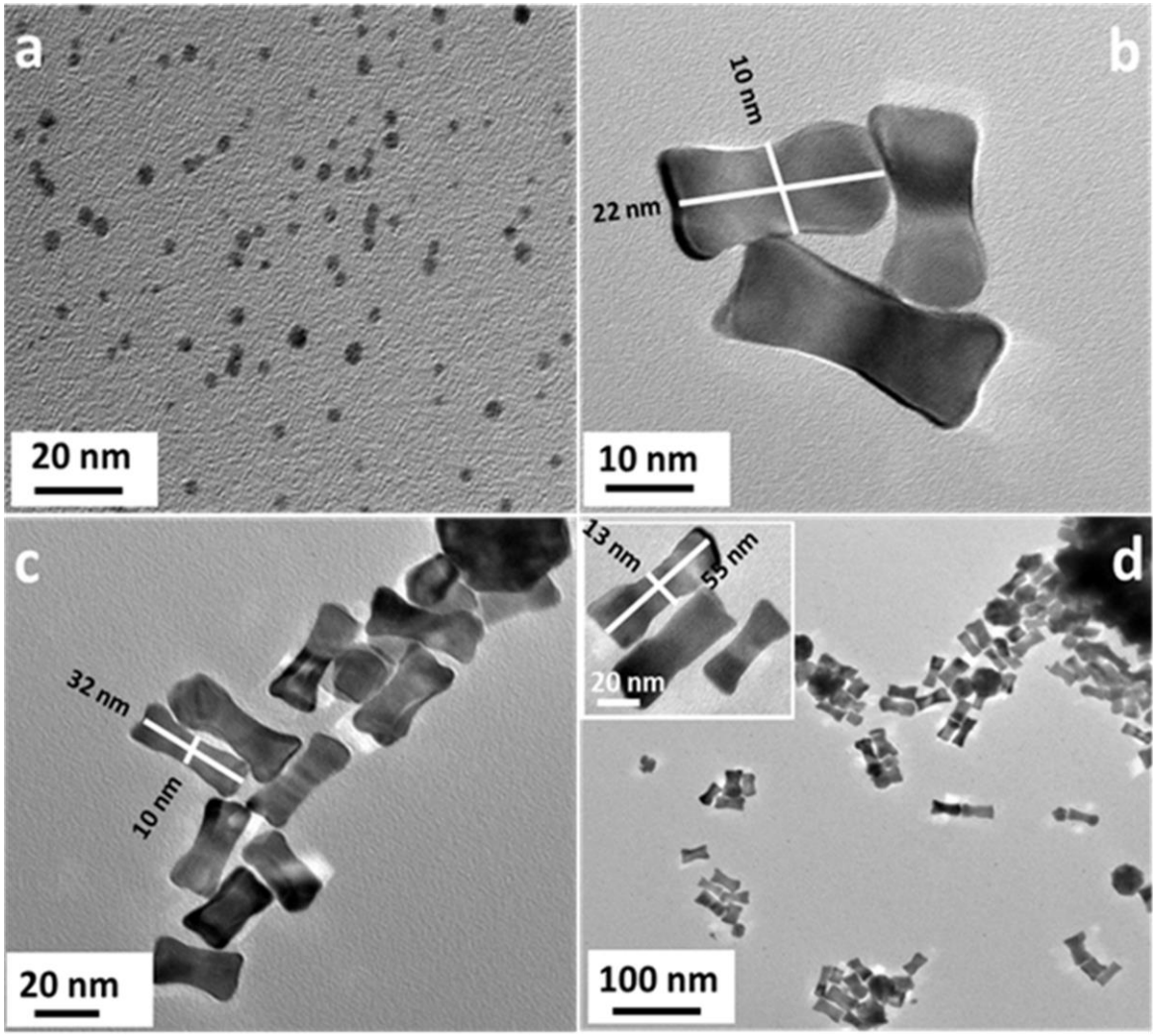

Figure 5.3. TEM images of representative gold dogbones of variable aspect ratio: (a) SP, (b) DNR 1, (c) DNR 3 and (d) DNR 6.

deposited preferentially onto the ends. With increase in concentration of $AgNO_3$ in the growth solution, the GDNR diameter remains nearly constant, while the length of the dogbones gradually increases.

Now, we have studied the emission behavior (λ_{ex}~ 535 nm) of sudan red 7B (0.3 µM) in the presence of GDNRs (20 µM) of variable aspect ratio as shown in Figure 5.4. In these experiments, quite dilute solutions have been used so as to minimize the effects of excitation attenuation and solution self-absorption (so-called 'trivial effects'). It is seen that the SR7B emission showed distinctly different emission profile in the presence of different sets of GDNRs and all sets of gold particles quenches the fluorescence of the dye molecules. However, no remarkable difference in the line shape of the emission

spectra of SR7B in the presence of the nanostructures was observed. A plot of relative efficiency, I_0/I where I_0 and I are the intensities of emission spectrum of the dye molecules in the absence and presence of GDNRs of variable aspect ratio is shown in Figure 5.5. The quenching efficiency varied ≤5% for a set of measurements from same batch of the nanorods and ≤7.5% from different batches prepared in different times. It is noted that the relative intensity decreases exponentially with increase in aspect ratio of rods, maximum being in case of ultrasmall spherical nanoparticles.

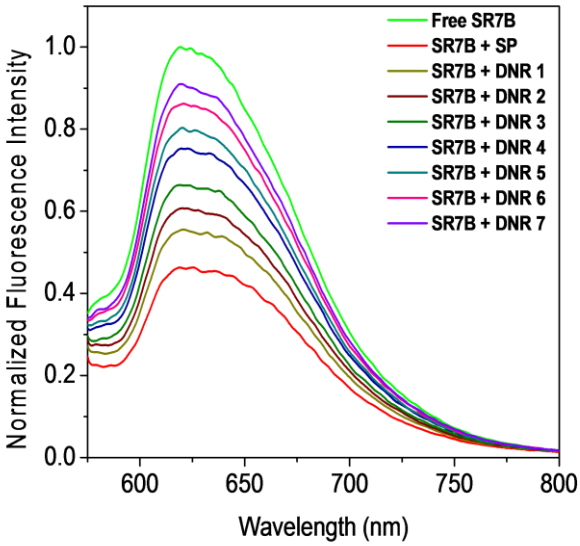

Figure 5. 4. Emission spectra of SR7B (0.3 µM) in the presence of GDNRs (20 µM) of variable aspect ratio.

The strongly confined fields near metallic nanostructures can modify the intrinsic fluorescence of nearby fluorophores.[24] The localized plasmon resonances of metal nanoparticles can confine light into nanometer regions and therefore, provide a platform for the control of light-matter interactions at the nanoscale. The quenching of molecular fluorescence near gold nanostructures could be treated within the framework of the model proposed by Weitz et al.[25] The increased electric field near metal nanostructures modify the fluorescence by increasing optical excitation rates by strengthening the local electric field, lowering the emission efficiency by offering non-radiative decay channels for the molecular dipole, and increasing the fluorescence by coupling radiative molecular emission to a radiative LSPR mode. The variation in intensity of the dye molecules reflects the number of SR7B molecules varies for different GDNRs. Several parameters, *viz.*, shape and size of the nanoparticles, distance between the excited-state molecules and nanoparticle surface, orientation of the molecular dipoles with respect to the nanoparticle surface plane, and overlap of the molecule's emission spectrum with the absorption

spectrum of the nanoparticle are known to influence the radiative and non-radiative decay kinetics of excited states near metal nanoparticles.[5] In the present experimental condition, the separation between nanorod surfaces and fluorophore (upon collision) is constrained by the thickness of the capping monolayer i. e., the molecular chain length of CTAB (~2.57 nm). There is, finally, no designed control over the orientation of the fluorophore molecular dipole relative to the GDNRs core surface and could be anticipated that molecules are statistically oriented at all possible angles onto the surface of the dogbones. Under this situation, the effect of the nanorods on the fluorescence quenching of the dye molecules could be rationalized by considering the interplay of size and shape and therefore, the surface area of the GDNRs. The gold nanorods do not exhibit fluorescence. When the fluoroprobe SR7B is allowed to interact with rods, a part of the dye molecules adsorbed onto the gold nanorods while the rest remain free in solution. Thus, the only fluorescing component is the free SR7B molecules in the solution and the observed emission spectra are due to the presence of unbound probe molecules in the system. As the aspect ratio of the nanorods decreases, the particles become smaller and there is a corresponding overall increase in surface area of the particles for a particular gold concentration. The increased surface area allows accommodation of a greater number of probe molecules around the GDNRs and hence smaller rods become more efficient quenchers of molecular fluorescence than the larger ones.[26]

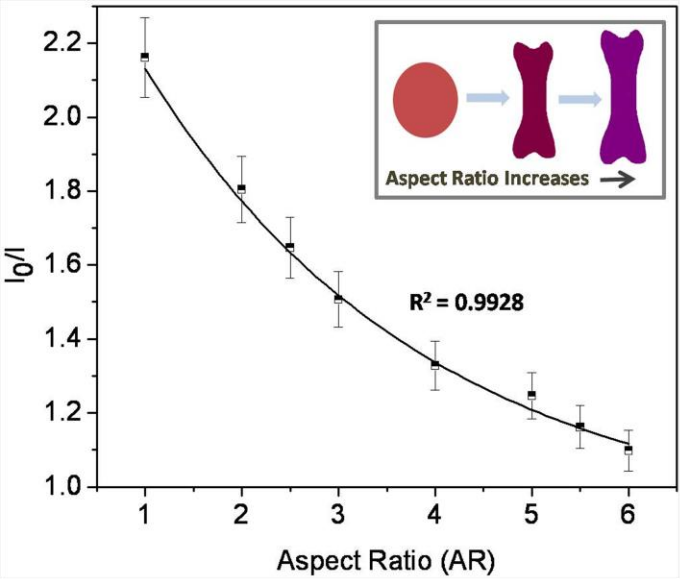

Figure 5.5. Profile showing the relative intensity of SR7B as a function of aspect ratio of GDNRs. Inset provides a schematic presentation showing aspect ratio gradually increases from spheres to larger dogbones.

In Figure 5.5., it is noted that spherical particles are superior quenchers of molecular fluorescence than the DNRs. This is due to the fact that for a gold spherical nanoparticle,

both radiative and nonradiative decay are enhanced around the plasmon resonance, but non-radiative decay clearly dominates, resulting in low quantum efficiency.[27] In the case of GDNRs, the longitudinal plasmon resonance energy of each dogbones is determined by the length-to-diameter aspect ratio, and they exhibit reduced plasmon damping compared to spherical gold nanocrystals.[27] Under the experimental condition, the aspect ratio of the dogbones are changed by keeping the diameter constant but increasing the length of the dogbones and the variation of relative intensity bears an exponential relationship with the aspect ratio of the nanorods. However, this is an empirical relationship under the experimental conditions and could not be generalized as the aspect ratio is the result of interplay of length and diameter of the nanorods. To obtain general relationship, the absolute dimension of GDNRs (i. e., length and diameter) should be taken into account rather than aspect ratio of the rods as the larger nanorods with same aspect ratio may have lesser quenching efficiency than the smaller nanorods.

Now, we have tried to elucidate the mechanism of quenching of molecular fluorescence upon interaction with the GDNRs. The successive changes of the absorption spectrum (0.25 mM) of gold nanorods (DNR 4) upon gradual addition of an aqueous solution of SR7B are illustrated in Figure 5.6 A. The consecutive changes of the surface plasmon band upon increase in the concentration of SR7B molecules indicate electron transfer onto the surface of GDNRs. The GDNRs produced, in thein the present experiment, prevents aggregation because CTAB stabilizes the particle surface as bilayer[28] around the surface of GDNRs, whereby the trimethylammonium head groups of the first monolayer are facing the nanorod surface and the absorbed second layer of CTAB extends outside the groups with positive charges through van der Waals' interactions between the surfactant tails[29] This formation develops a net positive surface charge due to the presence of adsorbed surfactant layers onto the nanorod surface. This layer is dynamic in nature and a continuous adsorption and desorption takes place in the system with the free CTAB molecules.[30] When fluoroprobe SR7B molecules are allowed to interact with rods, since the surface of the GDNRs are positively charged but not robust, the secondary amine group of the SR7B molecules are attached onto the nanorod surface through 'place exchange reaction'[31] as shown in the (bottom) inset in Figure 5.6A. Moreover, the gold atoms on the surface possess unoccupied orbitals for

nucleophiles to donate electrons. Therefore, the SR7B molecules containing amine functionality as the strong electron donors displace CTAB molecules from gold nanorod surfaces without any alteration in the morphology of the particles. Interestingly, it is observed that an increase in the concentration of SR7B molecules dampens the longitudinal surface plasmon band at 677 nm with successive red-shifting while the absorption at 530 nm increases indicating preferential binding of the dye molecules on the edges of the dogbones. This phenomenon will be accompanied with a change in the refractive index of the medium surrounding the particles which will further determine the

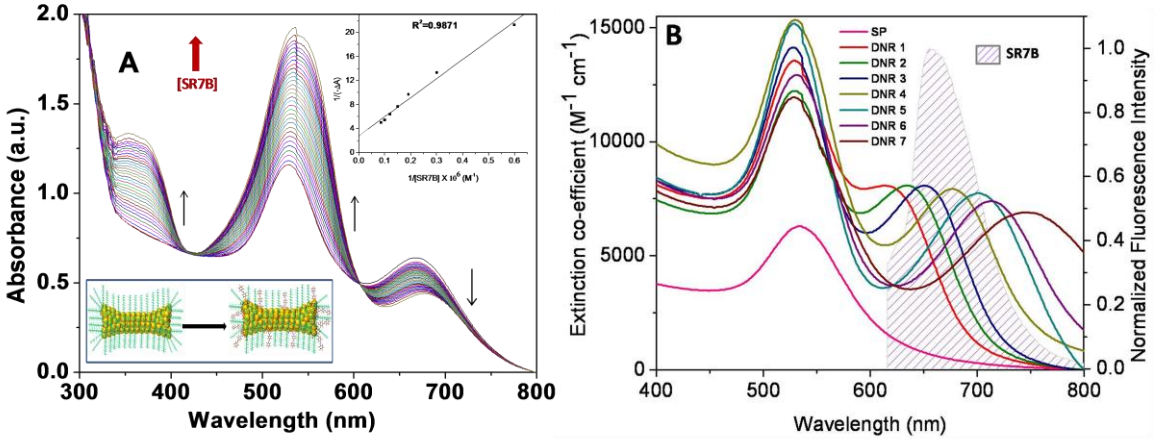

Figure 5. 6. (A) Surface plasmon band of DNR4 upon successive addition of SR7B. (Top) Inset shows the profile showing dependence of 1/(-ΔA) as a function of 1/[SR7B]. (Bottom) Inset shows a schematic presentation of the attachment of the dye molecules on the surfactant-stabilized of GDNRs. **(B)** Overlap between the absorption spectra of GDNRs of variable aspect ratio (0.25 mM) and emission spectrum of SR7B molecules (25 μM) indicating efficient energy transfer.

preferential shifting of the longitudinal plasmon band.[32] The electron transfer is pronounced for smaller nanorods as they have high surface area/energy and relatively more electronegative and therefore, possess high tendency to accept electrons. Therefore, smaller nanorods are effective quenchers of molecular fluorescence than the larger ones. The presence of an isosbestic point at 600 nm confirms that these absorption changes arise from a complexation equilibrium between the GDNRs and the dye molecules. The spectral changes observed in Figure 6A can be used to assess the apparent association equilibrium under the experimental conditions. The apparent association constant (K_{app}) for the complexation between GDNRs and SR7B was obtained by analyzing the

absorption changes similar to a Benesi-Hildebrand approach.[33] The double reciprocal plot of 1/(-ΔA) vs. 1/[SR7B] as shown in the (top) inset in Figure 5.6A gives an apparent association constant of 31.73×10^6 M^{-1}. The high value of K_{app} suggests a strong association between the dogbones and the SR7B molecules.

Quenching may also takes place when a fluorophore molecule is placed in a vicinity of a metal surface. When located near metal nanoparticles, excited fluoroprobes relax rapidly by exciting localized surface plasmons by means of near field coupling. The energy transfer is believed to be through the dipole-dipole near-field interaction which is known as Förster resonance energy transfer.[34] In the energy transfer process, the fluorophore acts as a dipolar donor, and the plasmonic GDNRs core functions as a dipolar acceptor. The probability of this Förster resonance energy transfer depends on the overlap of the emission band of the probe molecules with the absorption spectrum of the nanorods. Figure 5.6B shows the overlap between the absorption spectra of GDNRs and the emission spectrum of SR7B molecules. It is clear that the absorption of gold nanorods overlaps significantly with the SR7B emission, ensuring efficient energy transfer. In addition, strong plasmonic-molecular resonance coupling occurs between noble metal nanoparticles and organic fluoroprobes when the plasmonic resonance is degenerate with the molecular one. On a metallic surface, the nonradiative decay rate also increases for short fluorophore-metal distances, ~4 nm, since the non-radiative energy transfer rate depends on the inverse cube of the molecule-surface separation.[35,36] Due to chemisorption of the SR7B molecules to the gold surface, the molecular orbital of the probe molecules are mixed with metallic band states. Certain orbitals of SR7B interact strongly with the GDNRs and are responsible for chemisorption bond, while others are little affected by adsorption.[37] Thus, the energy transfer quenching is also very sensitive to the density of the electronic state changes.

In view of the above quenching mechanism, the fluorescence quenching of SR7B by GDNRs can be both static and dynamic. The former involves the formation of a non-fluorescent complex between the fluorophore and quencher in their ground states, whereas the latter requires diffusive encounters between the fluorophore and quencher during the lifetime of the excited state of the fluorophore. The Stern-Volmer equation accounting both static and dynamic (collisional) quenching could be written as,[38]

$$\frac{I_0}{I} = 1 + K_{SV}[Q] \quad (5.1)$$

where, $K_{SV} = K_S + K_D$. Here, K_S and K_D are the static and dynamic quenching constants respectively and Q is the quencher.

It has been seen that the fluorescence quantum yield of sudan red 7B does not change appreciably in the presence of experimental concentrations of the surfactant. Therefore, the adsorption onto the metallic surface of the dogbones could be ascribed to be responsible for the quenching of SR7B fluorescence. Figure 5.7 shows a plot of I_0/I vs. gold concentration at constant SR7B concentration for three different aspect ratio of the GDNRs. It is seen that the relative intensity shows good linear correlation with quencher concentration and corresponding K_{SV} values are determined as 9.08×10^3, 7.19×10^3 and 6.03×10^3 M^{-1} with aspect ratio 4±0.5, 5.0±0.5 and 6±0.7 respectively.[39] These results, quantitatively, authenticates that GDNRs with smaller aspect ratio are efficient quenchers of SR7B fluorescence than the larger aspect ratio nanorods.

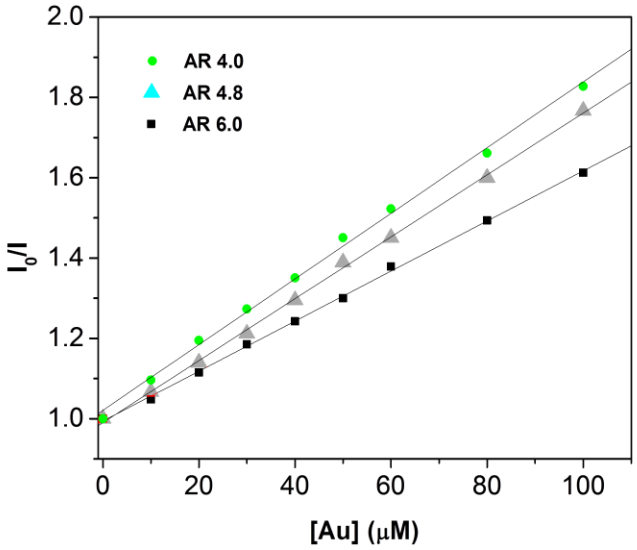

Figure 5.7. Stern-Volmer plot of relative intensity as a function of concentration of GDNRs of three different aspect ratio.

5. 1. 4. Conclusion

This sub-section directly provides an experimental verification of the effect of aspect ratio of dogbone-shaped gold nanorods on the emission behavior of molecular probe. Upon binding of the probe molecules onto the gold nanorods, the relative emission intensity decays exponentially with increasing aspect ratio of the nanorods. The fact that rods with lower aspect ratio are more efficient quenchers of molecular fluoroscence than higher aspect ratio rods is an important finding and this is due to higher surface-to-volume ratio of the smaller nanorods. Electron and energy transfer are considered to be the two major factors governing the process of deactivation of excited fluorophores onto the metal surface. It is anticipated that these results have significant implications for exploiting dogbone-shaped gold nanorods in a variety of optical and biotechnological applications.

5.2. Excess Surface Energy at the Tips of Gold Nanospikes

5.2.1. Introduction

Nanoscaled systems have become an active area of research in materials science, condensed matter physics, and chemistry because of their high surface-to-volume ratio and accordingly, the surface or interface energy is becoming the most important attributes in governing the physical and chemical properties of nanoscaled systems that may open new windows in technological applications.[40] As a result, thermodynamics of ultrasmall particles is becoming increasingly important as the dimension of electronic devices approaches the nanoscale. As the shape of the system deviates from isotropic spherical nanostructures, finding effective ways to deal with these systems has been a long-standing challenge. On the other hand, the ability of noble metal colloids to manipulate light at the nanoscale has pioneered an emerging research area called plasmonics.[41] In recent years, there has been tremendous progress over the past decade in the investigation of the shape-dependent properties of metallic nanocrystals and realization of their numerous potential applications in various fields, such as, electronics, photonics, or sensing.[42,43] Noble metal particles, *viz.*, copper, silver and gold, in the nanometer size regime exhibit strong absorption in the visible and NIR region, and this is indeed a small particle effect, since they are absent in the individual atom as well as in the bulk.[5,44] The dispersive electric field of the electromagnetic radiation causes collective oscillation of conduction electrons in metal nanoparticles with a resonance frequency, often coined as localized surface plasmon resonance (LSPR).[45] These collective oscillations of the conduction band electrons enable strong optical absorption and scattering in subwavelength structures, with spectral properties dependent upon the size, shape, interparticle interactions, dielectric properties, and local environment of the nanoparticles.[5,44] While the spectral properties of colloidal nanoparticles are, fundamentally, dependent upon their shape, the LSPR of anisotropic nanostructures could, easily, be tuned by controlling the morphology.[6] Gold nanospikes have been demonstrated to be highly promising class of shape-engineered nanoparticles as these multibranched nanoparticles with sharp tips display extremely interesting plasmonic properties with a broad surface plasmon band in the NIR region.[46-48]

The interdisciplinarity of plasmonics and thermodynamics has become a flourishing new field of science and technology offering a tantalizing opportunity to attain unprecedented levels of synergy between optical and electronic pursuances.[49] Organic dye molecules have often been used as local fluoroprobes to study the optical properties of noble metal nanostructures that are able to manipulate light at nanometer length scale.[8,50] Theoretical calculations and experimental observations have shown that, the main critical parameters, that modify the spontaneous rate of emission of organic dyes near metal nanoparticles are the location of the dye molecules around the particles, its separation from the metal surface, and the molecular dipole orientation with respect to the particle surface.[36] It is, now, well-established in the literature that, fluorescence of probe molecules is, usually, quenched in the vicinity of noble metal nanostructures but enhanced under restricted environments.[9] Beyond these critical experiments on nanospheroids, ingenious investigations have been put forward to study the photophysical aspects of molecular probes near anisotropic nanostructures, e. g., nanorods, nanocones, nanoshells etc.[12] Although the fundamental physics of the processes involved in metal-probe hybrid assemblies is quite matured, the non-local effect of anomalous surface energy of nanostructures has become the subject of immense investigation.[51] All steps of a surface chemical reaction–sticking, reaction and desorption–involve energy exchange between the adsorbate and substrate states. Therefore, it is essential to develop new theoretical tools for the understanding and determination of the surface energy distribution of the nanostructures and therefore, merging plasmonics and thermodynamics at the nanoscale.

In this sub-section, fluorescence spectroscopic technique have been employed in measuring the excess surface energy of the tips of gold nanospikes that play a pivotal role in governing the photophysical aspects of molecular probes near nanostructured metallic surfaces. Multispiked gold nanostructures have been chosen as the model systems as these possess different local environments around the nanostructures. We have employed alizarin red as the local probes to investigate the photophysical properties of the dye molecules near the anisotropic nanospikes in comparison with isotropic spherical nanostructures. It has been found that gold nanospikes are efficient quenchers of molecular fluorescence than the nanospheres due to morphological adversity in these anisotropic nanostructures. This hypothesis has, further, been validated by following the

temporal changes of molecular fluorescence during the photoconversion of the nanospikes into nanospheres under NIR laser irradiation. Based on the experimental realization of excess surface energy at the tips of the nanospikes, theoretical tools have been developed by geometrical modeling to calculate the excess surface energy around the nanostructures.

5.2.2. Experimental Section

5.2.2.1.Synthesis of Gold Nanospheres

Monodispersed gold nanospheres have been synthesized by seed-mediated growth method through the reduction of chloroauric acid using CTAB as the stabilizing agent[52] First,10 mL of aqueous $HAuCl_4.3H_2O$ solution (0.5 mM) was mixed with 0.6 mL aqueous solution of $NaBH_4$ (0.1 M) under vigorous stirring condition at room temperature for 10 min. The appearance of reddish brown coloration indicates the formation of gold seeds. Then, in the second step, 10 μL gold seeds has been added under stirring condition in a 25 mL growth solution containing $HAuCl_4.3H_2O$ (0.5 mM), CTAB (0.1 M) and L(+)-ascorbic acid (0.1 M) solution. The colorless solution, instantaneously, turns blue and subsequently, changes to pink within few seconds indicating the formation of larger gold nanospheres.

5.2.2.2. Synthesis of Gold Nanospikes

Multipod gold nanospikes have been synthesized through the reduction of chloroauric acid by following the recipe of Sau et al.[53] In a typical synthesis, 15 mL aqueous solution containing $HAuCl_4.3H_2O$ (0.9 mM), CTAB (0.6 M) and L(+)-ascorbic acid (4.0 mM) was taken in a conical flask at room temperature and mixed by 6-10 times gentle inversion after adding each reagent and capping the container. Then, requisite amount of aqueous $AgNO_3$ solution (20 μM) was slowly introduced along the slanted wall keeping the system, virtually, undisturbed. The colorless solution slowly developed a faint purple coloration, which rapidly changes to bluish, indicating the formation of multispiked gold nanoparticles in the solution. In this experiment, the concentration of $AgNO_3$ is judiciously selected in such a way that the number of the tips is fixed to 8-10.

5.2.2.3. Formation of Metal--Fluorophore Assembly

Gold nanospheres and nanospikes have been synthesized by following the procedure of Jana et al.[52] and Sau et al.[53] respectively. The as-synthesized gold nanospheres and nanospikes were centrifuged at 10,000 rpm for 10 min to remove the excess CTAB from the solution and re-dispersed into water by sonication. Then, various concentrations (0–40 μM) of gold nanospheres/nanospikes was added in an aliquot of freshly prepared aqueous solution of alizarin red (33 μM), incubated overnight under ambient condition (pH~7.0) to complete the surface complexation process and the fluorescence spectrum of each solution was measured in the spectrofluorimeter.

5.2.3. Results and Discussion

Alizarin red or 1,2-dihydroxyanthraquinone, also known as 'Turkey Red', is an organic dye belonging to alizarin family, derived from the roots of plants of the madder genus and has been used as a prominent red dye, especially, for dyeing textile fabrics.[54] Figure 5.8. shows the absorption and emission spectra of alizarin red in aqueous medium. The molecular structure of the dye is shown in the inset. The dye molecules exhibit a very intense absorbance band centered around 503 nm along with a less intense vibrational shoulder, centered around 307 nm corresponding to $n \rightarrow \pi^*$ and $\pi \rightarrow \pi^*$ transitions and molar extinction co-efficient, ε ~ 29,100 M^{-1} cm^{-1} corresponding to the monomeric form of the fluorophore.[55] Excitation at 503 nm

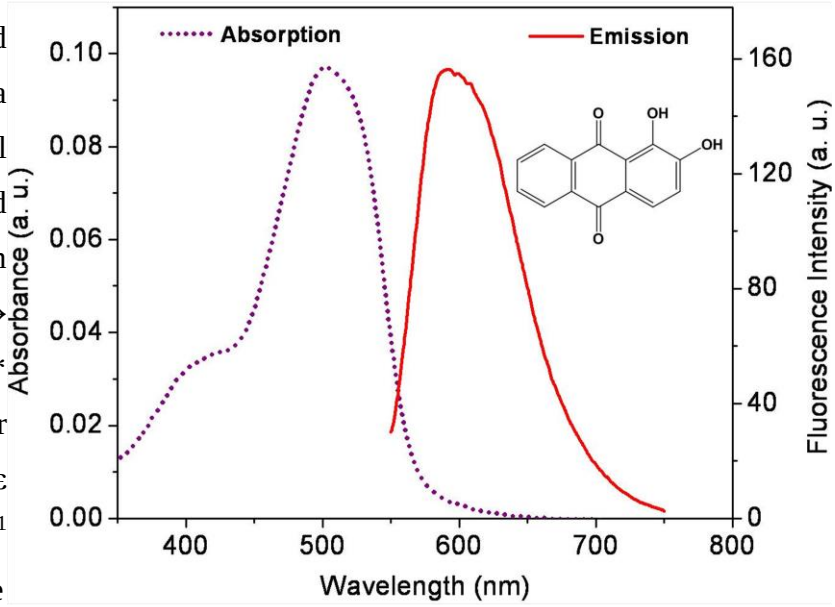

Figure 5.8. Absorption and emission spectra of alizarin red in aqueous medium. Inset shows the molecular structure of the dye molecule.

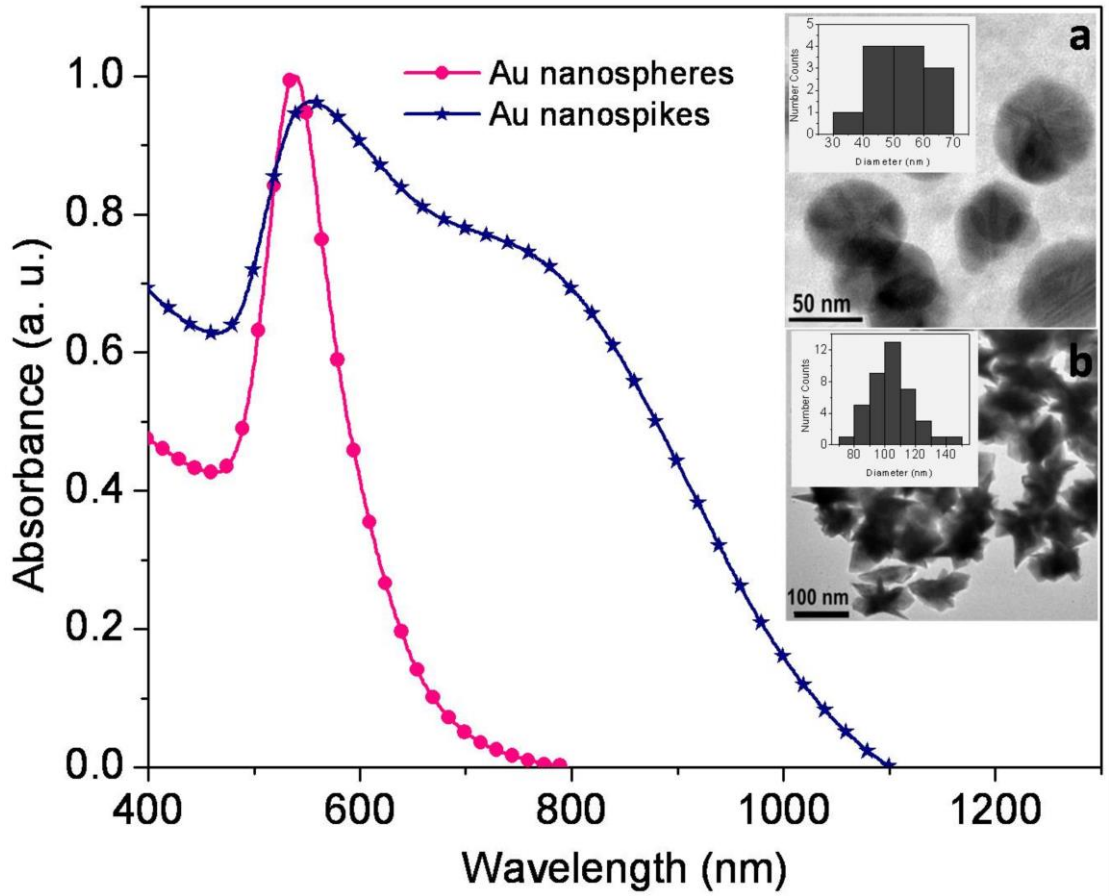

Figure 5.9. Absorption spectra of CTAB-stabilized gold nanospheres and nanospikes. Inset shows the transmission electron microscopic images (inset shows the corresponding diameter histogram) of gold (a) nanospheres and (b) nanospikes.

exhibit a broad emission spectrum with maximum intensity at 593 nm and quantum yield, $\varphi_f \sim 5.1 \times 10^{-4}$ corresponding to the neutral form of the dye molecules.[22] The emission spectra of alizarin red have been examined as a function of dye concentration in the range of 3 – 33 μM (not shown). It is found that there is no significant perturbation in the band structure and band position of the dye and fluorescence intensity (at 593 nm) increases linearly with increase in the concentration of the dye molecules indicating there is no significant dimerization or higher order aggregation in this concentration range. These well-suited photophysical aspects have enabled to study the emission characteristics of the alizarin red molecules with the metallic nanostructures.

The gold nanospheres[54] and nanospikes[22] have been synthesized by the methods described in the Experimental Section. Figure 5.9. represents the absorption spectra of gold nanospheres and nanospikes, respectively. It is seen that the nanosphere dispersion

displays a well-defined optical response with maximum at *ca.* 540 nm; this absorption band arises due to the localized surface plasmon resonance of spherical gold nanoparticles.[44] The absorption spectrum of gold nanospikes dispersion exhibit broad absorption band over the range of 500 – 1100 nm comprising of a short-wavelength plasmon band in the mid-visible region and a long-wavelength plasmon band in the NIR region with maxima at *ca.* 550 and 770 nm, respectively. These two bands could be attributed to the two dipolar resonance modes, which are assigned as localized within the central core and the multiple sharp tips of such particles, respectively. It has been shown that the plasmon of the gold nanostars results from the hybridization of plasmons of the core that serves as a nanoscale antenna, dramatically enhancing the excitation cross-section as well as the local electromagnetic field of the protruding prolate tips.[47,48] The plasmon spectrum of such particles shows a weak absorption around 520 nm that could be attributed to the plasmon resonance of the nanostar's core, and a dominant plasmon band at longer wavelengths due to the resonance supported by the nanostar branches.[48,56] Transmission electron microscopic images of gold nanospheres (image a) and nanospikes (image b) are shown in the inset. Transmission electron micrograph of the representative gold nanoparticles shows that the particles are nearly spherical with average diameter in the range of 55 ± 10 nm; the as-synthesized gold nanospikes comprise of quasi-spherical central part with sizes 50 ± 5 nm on the surface of which 8-10 shallow 'elliptical cone' shaped protrusions having relatively uniform hemiellipsoidal tips with sizes 40 ± 10 nm in length.

Now, we have performed comparative studies of the emission behavior of alizarin red (λ_{ex}~ 503 nm) in the presence of gold nanospheres and nanospikes as shown in Figure 5.10. In these experiments, quite dilute solutions (40 µM) have been used so as to minimize the effects of excitation attenuation and solution self-absorption (so-called 'trivial effects'). It is seen that the emission of alizarin red showed distinctly different profile in the presence of different concentrations of gold nanospheres (panel a) and nanospikes (panel b) and both the morphology of nanostructures quench the fluorescence emission of the dye molecules.

The salient feature of physical significance is that the extent of quenching is greater in case of gold nanospikes as compared to nanospheres provided that the concentration of gold remain constant. It is noted that quenching is much sensitive at the low concentration of gold nanostructures; for example, at 4 µM concentration, the quenching efficiency of gold nanospheres is nearly 20% while for nanospikes the corresponding value is 50% and both this value increases with increase in concentration of gold nanostructures. About 95% quenching efficiency is observed for gold nanospikes at the

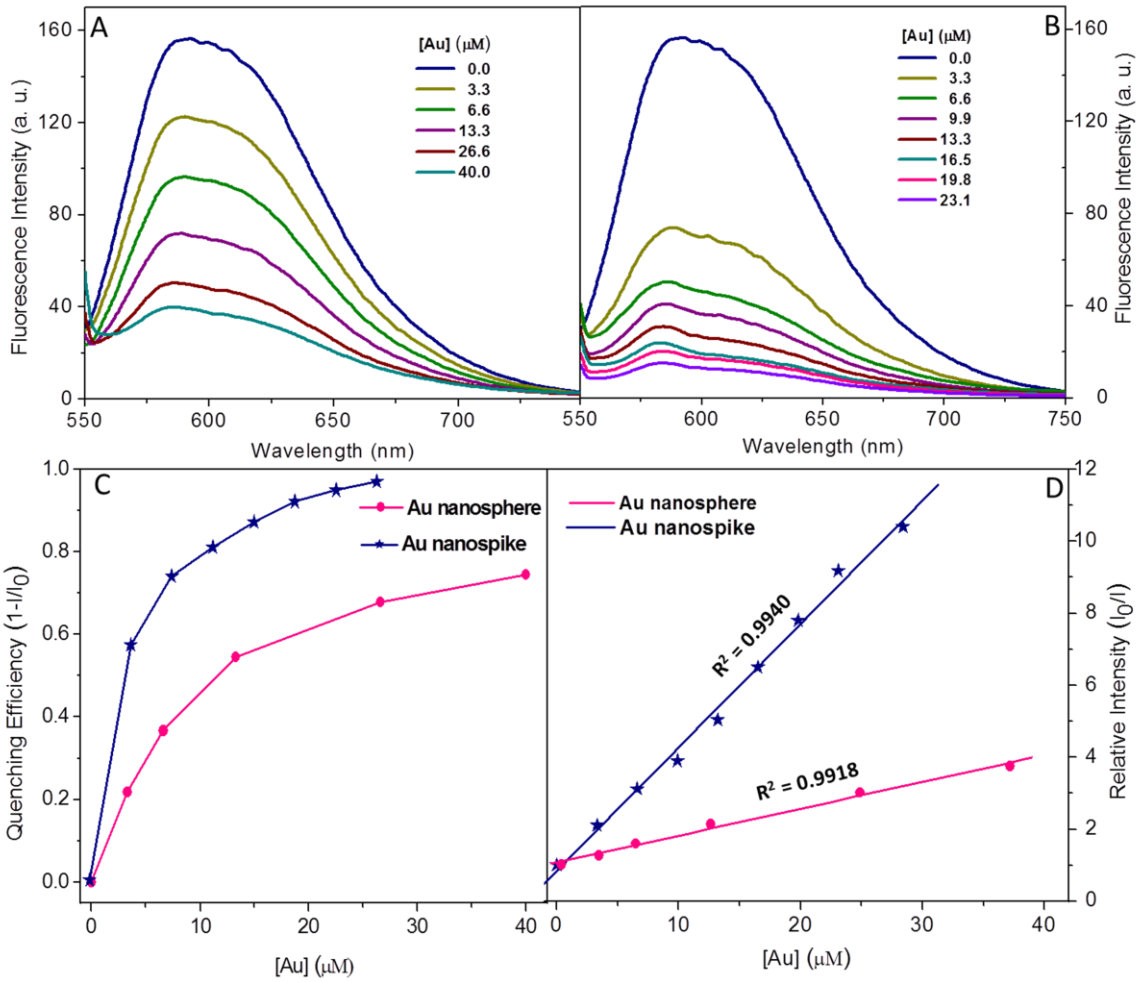

Figure 5.10. Emission spectra of alizarin red molecules (33 µM) in presence of different concentrations of gold (A) nanospheres and (B) nanospikes in aqueous medium; (C) Relative efficiency of alizarin red molecules in the presence of gold nanospheres and nanospikes and (D) Stern-Volmer plot showing the quenching efficiency of alizarin red as a function of concentration of gold nanospheres and nanospikes.

concentration of 20 μM but less than 80% quenching observed even at 40 μM of the nanospheres. Panel c shows a plot of relative quenching efficiency, $\theta = 1 - I/I_0$ as a function of gold concentration, where, I_0 and I are the intensities of emission spectra of the dye molecules in the absence and presence of the nanostructures as a function of gold concentration of the nanospheres and nanospikes. It is also noted that the relative quenching efficiency exponentially increases with increasing concentration of gold nanostructures. The quenching of molecular fluorescence in the vicinity of metallic nanostructures could be treated by the model proposed by Weitz et al.[25] A fluoroprobe in the vicinity of metallic nanostructures may be influenced by radiative and the non-radiative de-excitation rates involved in the fluorescence emission. Depending on its relative position and orientation with respect to the nanostructures, the fluoroprobe may experience an enhanced or suppressed electric field, leading to a higher or lower excitation rate, respectively, in comparison to a fluorophore in free space. In metal-fluoroprobe hybrid assemblies, the excitation of the electronic plasma resonance leads to an increase in the absorption rate. Again, the molecular emission dipole excites the plasma resonance leading to an increase in the rate of radiative decay while the non-radiative branch of the decay provides an additional damping effect. In the present experiment, it is observed that gold nanospikes are efficient quenchers of molecular fluorescence than the nanospheres. It is noted that the gold nanospheres/nanospikes are, themselves, non-fluorescent. When the fluoroprobes are allowed to interact with the nanospheres/nanospikes, a part of the dye molecules are adsorbed on its surface while the rest remain free in solution and thus, the only fluorescing components are the free alizarin red molecules in the solution. The K_{SV} is related to the photoluminescence efficiency via the relationship of the Stern-Volmer equation[57] accounting both static and dynamic (collisional) quenching as,

$$\frac{I_0}{I} = 1 + K_{SV}[Quencher] \qquad (5.1)$$

where, $K_{SV} = K_S + K_D$. Here, K_S and K_D are the static and dynamic quenching constants respectively. Panel d shows the profiles of I_0/I *vs.* gold concentration for a fixed concentration of alizarin red (33 μM) for both the morphology of the nanostructures and corresponding K_{SV} values are determined as 0.7263×10^5 and 3.4297×10^5 M^{-1} for gold nanospheres ($R^2 = 0.9918$) and nanospikes ($R^2 = 0.9940$), respectively. It is noted that,

the *Ksv* for gold nanospikes is, surprisingly, about five-fold higher than the nanospheres, provided that all the other relevant parameters, like, size of the particles and the structure of the stabilizing ligand shell remain almost invariant.

Now, we have tried to elucidate the mechanism of quenching of molecular fluorescence upon interaction with the gold nanostructures. Both electron and energy transfer processes contribute to the major deactivation pathways for excited fluoroprobes on the metal surface as has been elucidated in Figure 5.11. Panel A shows the absorption spectral changes of gold nanospikes upon successive addition of alizarin red. Inset shows the corresponding changes of the gold nanospheres upon addition of the dye molecules. When alizarin red molecules are added to the gold nanospikes, the broad longitudinal plasmon band of gold nanospikes gradually dampens with increase in concentration of alizarin red while an enhancement of the transverse plasmon band with concomitant blue shift is seen. A closer observation shows that the absorption intensity of alizarin red molecules increases the intensity of transverse plasmon band due to sum of the surface plasmon band of gold nanostructures and absorption band of the dye molecules. This effect is observed at the transverse plasmon band region with increasing concentration of alizarin red at a particular concentration of gold nanostructures; similar change in the plasmonic features of gold nanospheres is seen upon addition of the dye molecules. These results imply electron transfer from the dye to the gold nanostructures and points out that the tips of the nanospikes have different electronic environments than the spherical region.[58] Panel B shows the overlap between the absorption spectrum of gold nanospheres/nanospikes and the emission spectrum of alizarin red molecules ensuring efficient energy transfer. Fluoroprobes placed in the vicinity of gold nanostructures can transfer energy to the nanospheres/nanospikes once it gets excited. The energy transfer is believed to be through the dipole-dipole near-field interaction, where the fluorophores act as dipolar donors and the plasmonic gold nanostructures act as dipolar acceptors. The probability of this Förster resonance energy transfer is proportional to the spectral overlap between the absorption of the metallic nanostructures and the fluorescence emission of the probe molecules. The overlap integral between the donor emission and acceptor absorption could be written as,[59]

$$J(\lambda) = \frac{\int_0^\infty F_D(\lambda)\varepsilon_A(\lambda)\lambda^4 d\lambda}{\int_0^\infty F_D(\lambda)d\lambda} \qquad (5.2)$$

where, $J(\lambda)$ is the overlap integral, $F_D(\lambda)$ the fluorescence intensity, $\varepsilon_A(\lambda)$ the extinction co-efficient expressed in M^{-1} cm^{-1} and λ the wavelength in nanometers. The calculated overlap integral of donor, alizarin red to acceptor, gold nanospheres and nanospikes have the value of 5.9223×10^{14} and 1.1335×10^{15} M^{-1} cm^{-1} nm^4 respectively. It is noted that overlap integral of gold nanospikes is about two-fold higher than the nanospheres; therefore, it is apparent that on the view point of energy transfer nanospikes are doubly efficient quenchers of molecular fluorescence than the nanospheres.[60]

Based on the electron transfer mechanism, this apparent difference in the fluorescence quenching efficiency could be anticipated to the enhanced surface area that would allow the excess accommodation of alizarin red molecules on the gold nanospikes. The calculation of total number of particles and hence, the total surface area for a particular gold concentration could provide certain attributes to explain the difference in the fluorescence quenching efficiency due to the presence of anisotropy in the nanostructures. The number concentration (number of particles per milliliter of the solution, N) of gold particles can be calculated by taking the ratio of total volume of the

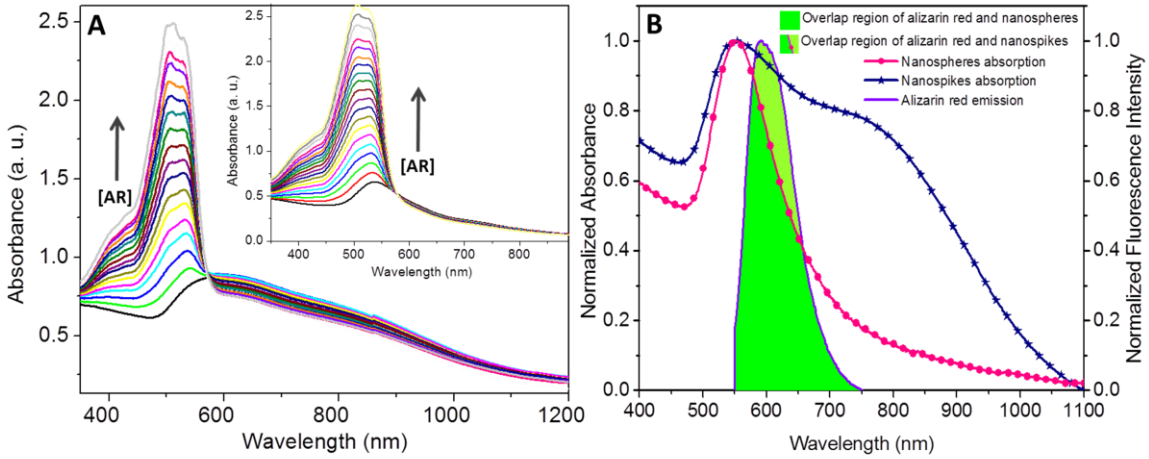

Figure 5.11. (A) Absorption spectral changes of gold nanospikes (0.25 mM) upon successive addition of alizarin red. Inset shows the corresponding changes of the gold nanospheres upon addition of the dye molecules. (B) Overlap between the emission spectrum of alizarin red (33 µM) with absorption spectra of gold (0.25 mM) nanospheres and nanospikes.

atoms to the effective volume of each particle taken in average. The approximate numbers of nanospheres and nanospikes per milliliter of the solution have been calculated using the formula,

$$N = \frac{N_0 C}{1000 f}\left(\frac{r}{R}\right)^3 \quad (5.3)$$

where, N_0 is the Avogadro's number, C the concentration of the gold precursor, f the packing fraction of the atoms in the nanostructures, r the radius of gold atoms, R the average radii of the particles. Assuming the packing fraction as 0.74 for fcc gold[61] and a precursor concentration of 1.0 mM, the number concentration of the nanospheres and nanospikes are, approximately, 8.85×10^{10} and 4.91×10^{10} mL^{-1} respectively. The corresponding surface area per nanostructure is, approximately, 9852.03 and 21855.88 nm^2 respectively and total available surface area is 8.71×10^{14} and 10.73×10^{14} nm^2 mL^{-1}, respectively. Thus, the total available surface area is *ca.* 1.2 times higher for nanospikes compared to nanospheres. It is, therefore, apparent that the quenching efficiency does not scale linearly with the surface area of the nanostructures; some other factors beyond the surface area are complementary for the fluorescence quenching of the probe molecules in the presence of the anisotropic nanospikes compared to spherically symmetrical gold nanostructures.[9] Thus, it could be conceived that the excess surface energy at the tips of the nanospikes may be responsible for the additional quenching of the molecular probes near the anisotropic nanostructures. To substantiate the additional role of the tips of the nanospikes in fluorescence quenching of the molecular probes, we have observed morphological and spectral changes of the gold nanospikes as a function of heat treatments (Figure 5.12). In this experiment, gold nanospikes were excited with 785 nm laser that coincides with and therefore, excites the longitudinal plasmon absorption and photoinduced shape transformation has been monitored in real time by UV-vis-NIR spectroscopy. Before irradiation, the spectrum shows two well-resolved bands centered at *ca.* 550 and 770 nm respectively. Upon increase in irradiation time, it is seen that while the longitudinal plasmon band showed a substantial decrease in its absorbance and a pronounced blue shift, the intensity of the transverse plasmon band

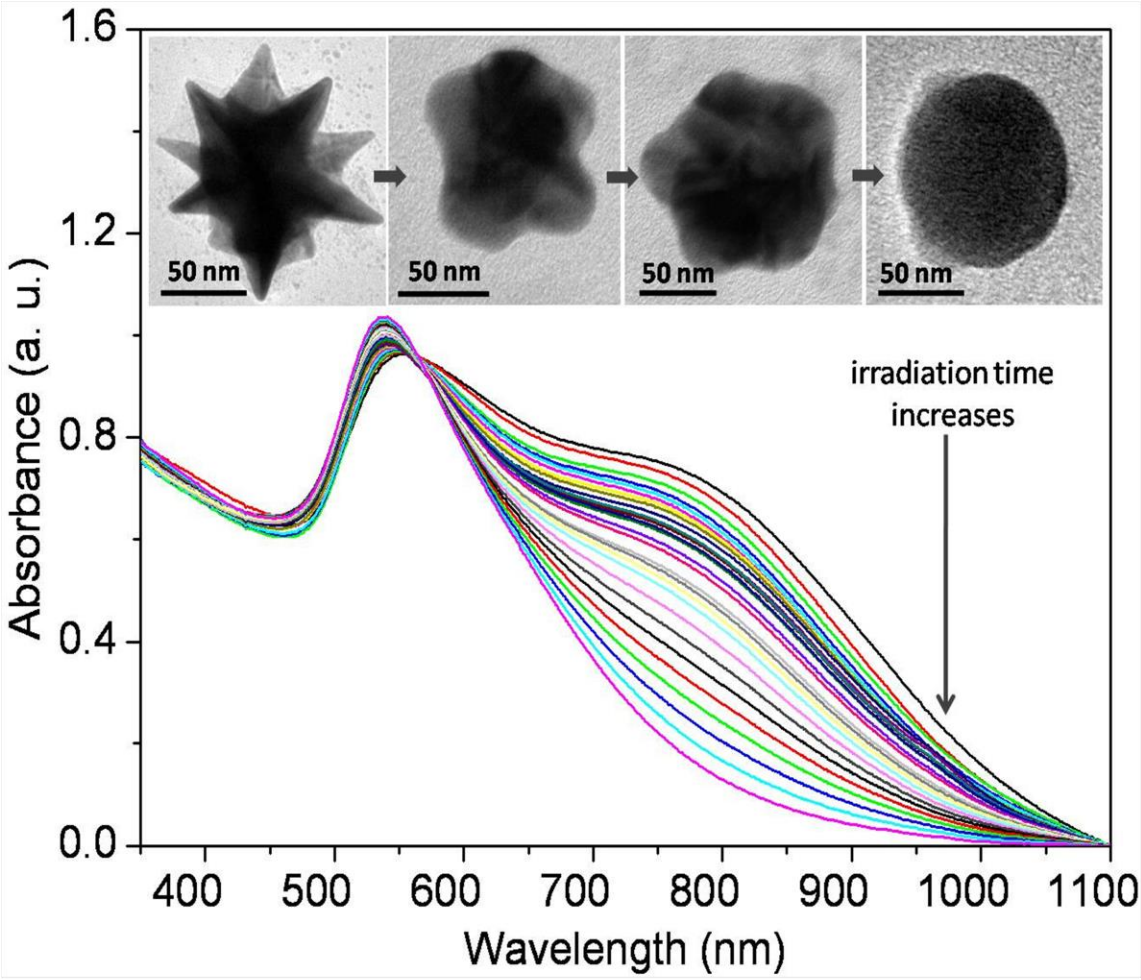

Figure 5.12. Temporal changes in the absorption spectral features of gold nanospikes upon NIR laser irradiation. Inset shows the transmission electron micrographs during the photoirradiation of gold nanospikes to nanospheres at different stages of irradiation.

consequently increases. A single absorption band at 550 nm was recorded after 24 h of reaction, and no more changes to the spectrum were further seen. The subsequent changes of the nanostructures can be easily visualized by a gradual change in the solution color from deep blue to purplish blue to pink to red with the progress of the irradiation. These spectral changes indicate that the spikes are melting down and this process is continued up to complete the conversion to spheroidal nanostructures.[62] It is also noted that the transverse mode of the plasmon absorption of gold nanospikes is less intense than the surface plasmon absorption of spherical gold nanoparticles and therefore, during the photoconversion, the intensity of the transverse plasmon band of the nanospikes slowly becomes engulfed by the overwhelming intensity of the quasi-spherical to spherical

nanostructures.[63] Real-time monitoring of the photoconversion process suggests a strong dependence of the particle spectral response on the specific corner features of the colloidal nanostructures as shown in the inset. Initially, it is seen that the nanospikes possess numerous well-defined longer and sharper tips relatively uniformly on the gold surface (panel a). Upon irradiation, the branches taper off at the ends and form relatively short and obtuse branches (panel b). Further irradiation shows that the branched corners are more rounded resulting minuscule edge length that could be considered as part of the surface roughness and not as branches (panel c). Finally, spherical nanoparticles are evolved indicating that gold nanospikes and completely transformed into spheres after exposure to the laser pulses. These results suggest that the restructuring of the spikes starts from the top of the tips indicating high surface energy at the apex of the nanospikes.[64]

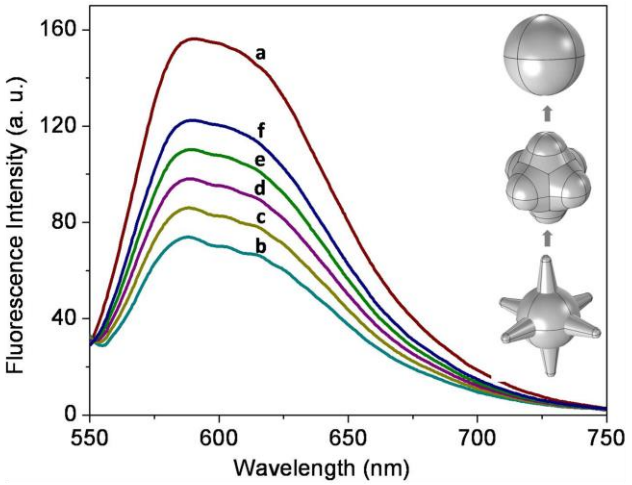

Figure 5.13. Emission spectra of alizarin red (33 μM) in the presence of different morphology of gold nanostructures evolved during the photoirradiation of gold nanospikes to nanospheres. Inset shows a schematic presentation of the three-dimensional geometrical modeling of the illustration of the particle shape evolved during laser irradiation.

In order to precise the influence of these intricate gold nanostructures, the emission behavior of alizarin red (λ_{ex}~ 503 nm) has been studied in the presence of different gold nanostructures evolved at different times of irradiation as shown in Figure 5.13. It is seen that the emission of alizarin red showed distinctly different profile in the presence of gold nanostructures evolved during the morphological transformation of nanospikes to nanospheres. Interestingly enough, it is observed that the quenching efficiency is maximum in case of gold nanospikes, gradually decreases with decrease in length of the tips and minimum for the ultimate spherical particles. It is seen that the immediate vicinity of the tips of the spikes exhibit regions of high surface energy that is attributable to the lack of symmetry at the interface or to the confinement of electrons

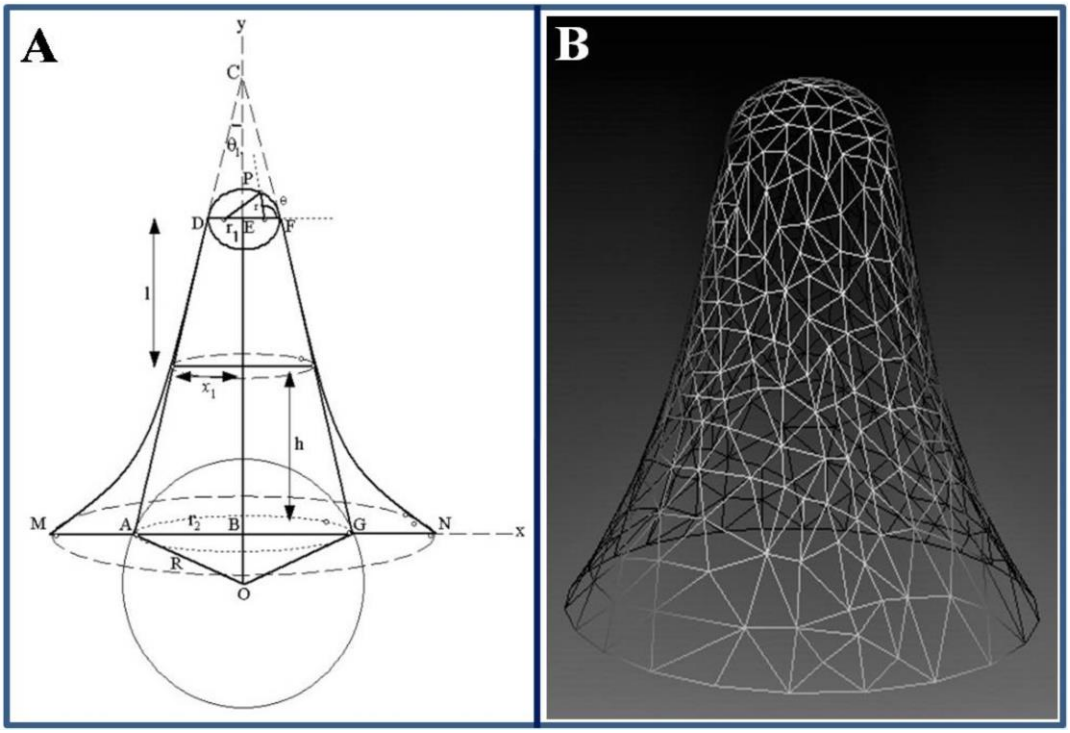

Figure 5.14. Exponential growth of the protruded arm: (A) two-dimensional geometrical model and (B) corresponding three-dimensionally rendered structure.

that does not scale linearly with size;[65] as a result, with decrease in the sharpness of the tips, the quenching efficiency decreases. Therefore, it could be authenticated that the excess surface energy near the tips of the spikes plays an important role in adsorption and quenching the fluorescence of molecular probes.

In this context, we have attempted to derive the excess surface energy onto the tip of a nanospike followed by exact determination of the excess surface area. We have employed basic Euclidean geometry to calculate the surface area of nanostructures, highlighting on the solid cone formed by the protruded extension of the spike.[66] A two-dimensional geometrical model (panel A) and the corresponding three-dimensionally rendered structure of a protruded arm (panel B) are shown in Figure 5.14. Based on the two-dimensional geometrical model (panel A) the nanospike could be assumed to be consisting of a ellipsoidal tip-head (surface area A_e) designed from the real-time TEM image of the tip, and the prolonged conical arm (surface area A_{cone}) protruded out from a basal spheroidal core (A_{core}) which creates a polynomial surface on protrusion base (surface area A_p).

Calculation of Surface Area of the Nanospike. Figure 5.15 shows the hollow bottom protrusion on a spherical core and simplified 2D projection of a protruded cone onto a spherical core. Panel a shows the simplified model which consists of a spherical core having radius *R* with a tangential protrusion in a planar projection. For a more simplified view to this problem, let us assume that, for any given blunt cone, the cross-sectional radius of the cone (r_1) is constant, which implies that, the points G and H will be fixed, and with the change in angle, θ_1 the top point C move along y-axis. In this regard, it is worth to mention that the maximum limit of angle θ_1 is 45°, which is one of the boundary conditions applied throughout the calculation. Considering panel b,

$$r_2^2 = R^2 \cos^2 \theta_1 \tag{5.4}$$

Now, for surface area of the spherical core, we have, $dA_{core} = R^2 \sin^2 \theta d\theta d\phi$

Therefore, for spikes having the unchanged spherical core radius, in terms of θ_1, the relationship becomes,

$$-dA_{core} = 2\pi r_2^2 d\theta_1 \tag{5.5}$$

This equation, thus, depicts the decrease of the surface area of core sphere for each of the cone placed onto the surface of the sphere. The surface area of a hollow bottom cone can be given by, $A_{cone} = \frac{2\pi r_1 l}{\cos\theta_1}$. Thus, change in surface area of the cone depends on both the half open angle, θ_1 and the difference between top and bottom radii, Δr as,

$$dA_{cone} = 2\pi\left(\frac{\Delta r}{\sin\theta_1} dr_1 + \frac{r_1 \Delta r}{\cos\theta_1} d\theta_1\right) \tag{5.6}$$

Therefore, the change in surface area can be estimated if, we

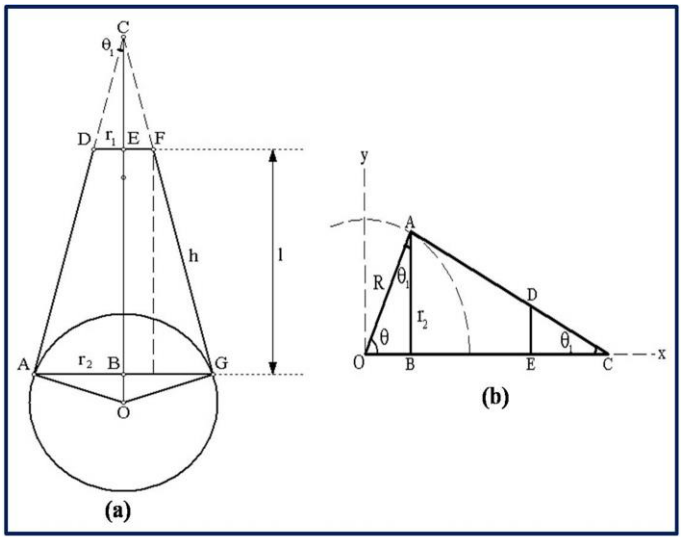

Figure 5.15. (a) Hollow bottom protrusion on a spherical core and (b) simplified 2D projection of a protruded cone onto a spherical core.

consider a spherical cross-section of radius r_2 with respect to the tip radius r_1 and inclination angle. But, in practice, a smooth protruded base is found in real spikes when the open angle, θ_1 is narrower than tangential arrangement. The 2-D model of the protruded arm in panel A is based on the consideration that the continuous growth of the arms up to height *h* as a exponential function to the y-axis as, $-x = \exp(sy)$ where, *s* is the steepness factor and could be obtained by taking a tangent at the mid-point of the arc.

The arc length, C is given by,

$$C = \frac{(y - z) - (\tan^{-1} y - \tan^{-1} z)}{s} \tag{5.7}$$

where, $y = \sqrt{s^2 \exp(2sh) + 1}$ and $z = \sqrt{s^2 + 1}$. If the top radius of the fulcrum is x_1, the surface area is given by,

$$dA_p = x_1 C d\phi \tag{5.8}$$

Again, the surface area of the blunt edge (A_e) at the protrusion end could be modeled by hemi-spheroidal surface cap having semi-major axis, *a* and semi-minor axis, b. The hemi-spheroidal surface can be of two types, *viz.* prolate and oblate and corresponding surface area can be given by,

$$\left.\begin{aligned} A_{prolate} &= 2\pi b\left(b + a \times \frac{\arcsin e}{e}\right) \\ A_{oblate} &= 2\pi b\left(b + a \times \frac{\sinh^{-1} e}{e}\right) \end{aligned}\right\} \tag{5.9}$$

where, $e = 1 - \frac{b^2}{a^2}$.

Therefore, by this anatomical modeling, we have simplified the complex geometry of a nanospike by a combination of basic geometrical counterparts. The present protocol could be applied to imitate any asymmetric nanostructure by fragmentation to the geometrical analogues which inherit the local symmetry among the overall structural asymmetry.

Therefore, the overall surface area could be expressed as,

$$dA = dA_p + dA_e + dA_{cone} + dA_{core} \tag{5.10}$$

For a given particle, the parameters could be measured accurately from a TEM image and thereby, the surface area could be calculated accordingly. Exploring the geometrical modeling through computational analysis and further modifying the vertices corresponding to the protrusion with Bezier polynomial surface in Meshlab®, a three-dimensional model of a protruded arm has been generated (panel B) which replicates the exact geometry and thereby, could be exploited to determine the surface area of such complex geometrical nanostructures.

Now, excess surface energy at the tips depends on the sharpness of the tip which depends on the ellipticity (*e*) of the projected segment of the ellipsoidal tip. Hasley[67] derived the corrected form for BET isotherm depending on the radius of curvature of the surface as,

$$\Gamma = (\frac{r}{r+1})^{1/r} \tag{5.11}$$

Menger and Rizvi[68] have shown that, for a rough surface, the change in surface tension depends on the radius of curvature of the surface as,

$$\gamma - \gamma_0 = \Gamma_{max} RT[\ln(1 - \frac{\Gamma}{\Gamma_{max}}) - \frac{k}{2}(\frac{\Gamma}{\Gamma_{max}})^2] \tag{5.12}$$

where, (γ - γ_0) is the difference in surface tension between the flat and bent surfaces, the intermolecular interaction coefficient, *k* is negative for cohesive energy.

Considering the polar form of the elliptical tip invoking appropriate boundary condition, we get,

$$\frac{1}{\Gamma_{max}} \frac{d\gamma}{dr} = RT(\frac{2r}{r^2+1} + kr) \tag{5.13}$$

Thus, surface energy per unit area of surface coverage at the tip, could be defined as,

$$\frac{E_{surface}}{\Gamma_{max}} = \frac{1}{\Gamma_{max}} A_e \int d\gamma \tag{5.14}$$

Now, in this equation, substituting the value from equation (7), the surface energy on tip (E_{tip}) could be expressed as,

$$E_{tip} = A_e(\theta, e).\gamma(r) \qquad (5.15)$$

where, $\gamma(r) = RT[\ln(r^2+1) + \frac{kr^2}{2}]$

It is noteworthy that, surface energy on the tip could be expressed as the product of two separable functions, of which the first part shows the angular dependence and the later part shows the radial dependence. A profile showing the radial dependence (r) of surface energy (E) and solvent interaction energy parameter (k) is shown in Figure 5.16. The plot shows exponential increase of surface energy on the increase of the radius of curvature of the ellipsoidal tip, which is dependent on the semi-major and semi-minor axis of the ellipse.

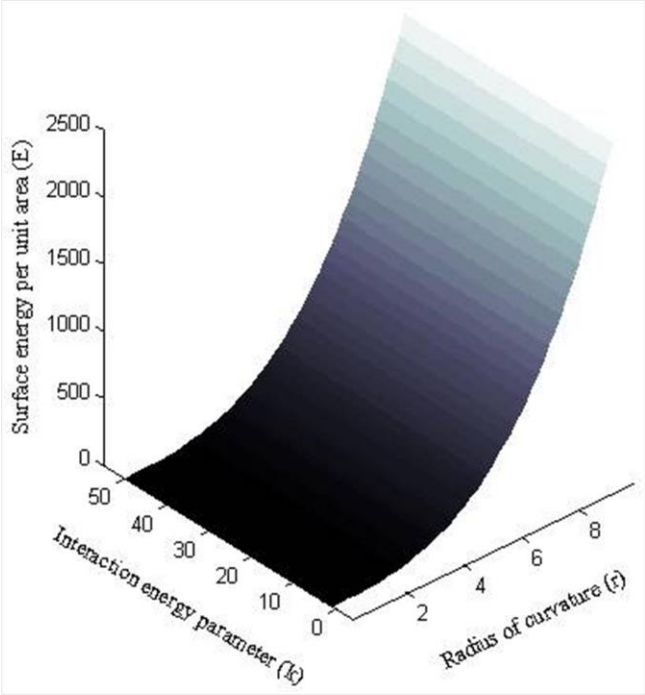

Figure 5.16. Plot showing relationship between surface energy (E), solvent interaction energy parameter (k) and radius of curvature of the tip (r).

The real-time modeling of tip of a nanospike can be achieved by taking the intersection of a plane with a solid cone. Depending on the symmetry of the tip, two plausible ways of modeling the nanospike are depicted by pictorial representation as shown in Figure 5.17. While panel A shows a solid cone with parallel planar intersection which results in a circular disk, panel B shows elliptical intersecting disk due to the non-parallel planar intersection with the solid cone. As a compromise, panel C shows the evolution of a conic section, which satisfies all through the points of intersecting planes and passes through the tip point. The spherical womb inside the solid cone is pruned to form a hemispherical tip, which is the most symmetric form of the system and thus, interpret the deviation from the ideal in each cases. The apex of the conic is slightly tilted from the apex of the parent cone and could, satisfactorily, be employed to devise the

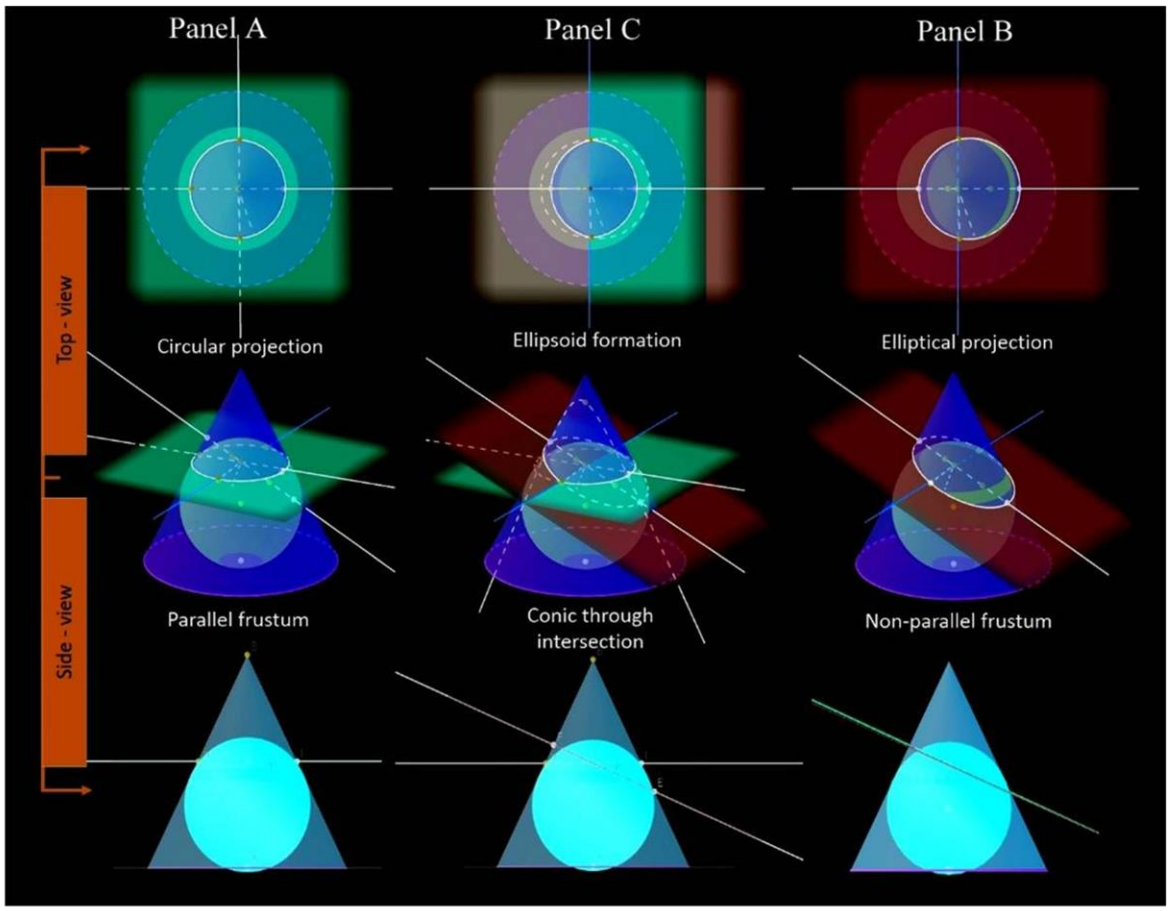

Figure 5.17. Modeling of the tip of a spike on the basis of intersection with a plane: (panel A) symmetric and (panel B) asymmetrical inclination of the cone, (panel C) the evolution of the conic section describing a general shape of the non-spherical cap.

three dimensional structure of the tip of a nanospike by invoking suitable boundary circumference of the conic section.

To employ the aforementioned technique in finding out the surface energy on the tip of a nanospike, two parallel planes were intersect which are perpendicular to apex of the tip (plane MPNQ, red) and basal plane (plane APCQ, blue) owing to form a straight line, PQ. Figure 5.18 shows the theoretical three dimensional model (panel A), corresponding anatomy of its two dimensional projection (panel B) obtained from the TEM image and three dimensional meshgrid (panel C) of the rendered model of tip. Transmission electron micrograph of a singular tip was scaled with ImageJ® software package; it was found that the average length of tip varied from 37 to 47 nm. Then, the tip head of the protruded arm was modeled using the derived theoretical calculations. The major and minor axis of the

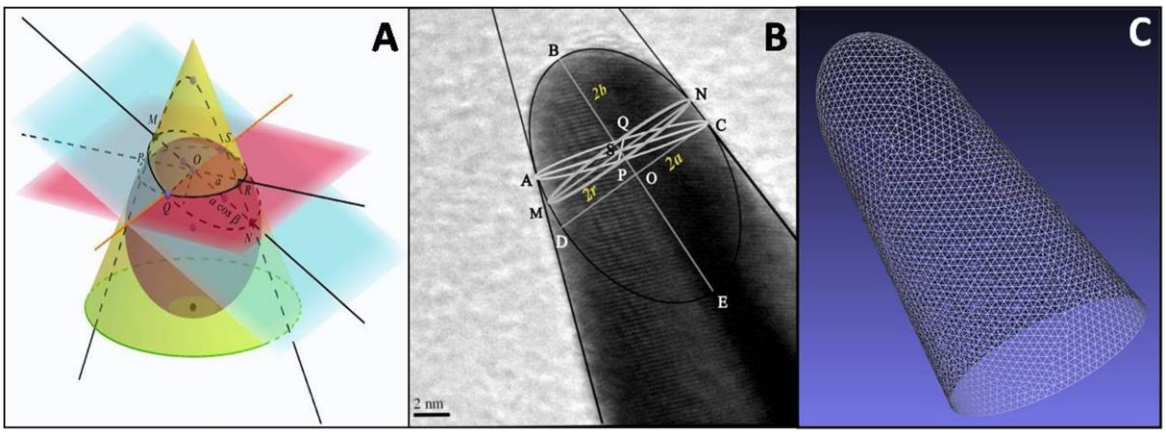

Figure 5.18. Three-dimensional modeling of the tip of a spike: (A) theoretical model, (B) transmission electron micrograph and (C) three-dimensional meshgrid of the rendered model of tip.

elliptical fit was found *ca.* 10 and 15.4 nm, respectively. Based on these measurements, we have employed theoretical perspectives to produce the three-dimensional protrusion with FreeCAD® and Meshlab® software packages. It is seen that the evolved structure has almost equivalent mesh triangulation over the whole surface and the corresponding surface area *ca*. 20,700 nm^2 which has ~5% relative error from the value obtained experimentally. The excess surface area with increase in protrusion of the tip has been modeled with respect to the increase in semi-major axis (c) for the tip ellipsoids with elliptical and round cone as shown in Figure 5.19. From the TEM image, overall spread of the radius of resultant nanospheres varies in the range between 22.5 nm to 32.5 nm, having a maximum at 25 nm. We, therefore, calculated the mean difference in

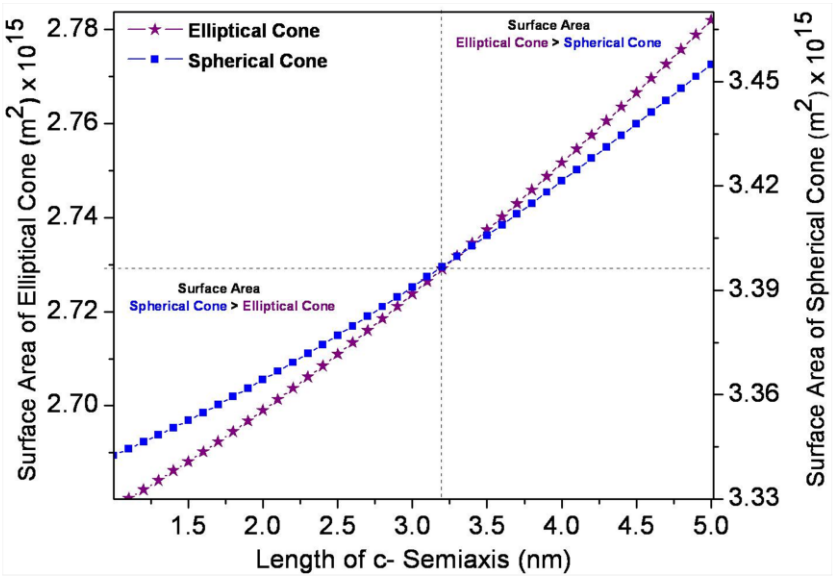

Figure 5.19. Change in surface energy of a tip ellipsoid as a function of perpendicular semi-axis.

surface energy for the overall spread from the modeled nanospike, and plotted the function with the increasing particle radius as shown in Figure 5.20. Both of the attainable geometries considered in Figure 5.19. show two feasible ways of atomic aggregation in the nanostructures and pass through a common point of equal surface area when the c-semiaxis is ~3.25 nm long. Afterwards, the surface area ofelliptical cones becomes wider than for conical shaped tips, which provide a measurable account for tip shape with respect to the height of tip head. With the increase in the length, the tip becomes narrower with circular base, which minimizes the extra surface energy that has taken into consideration in the modeling of the nanospike.

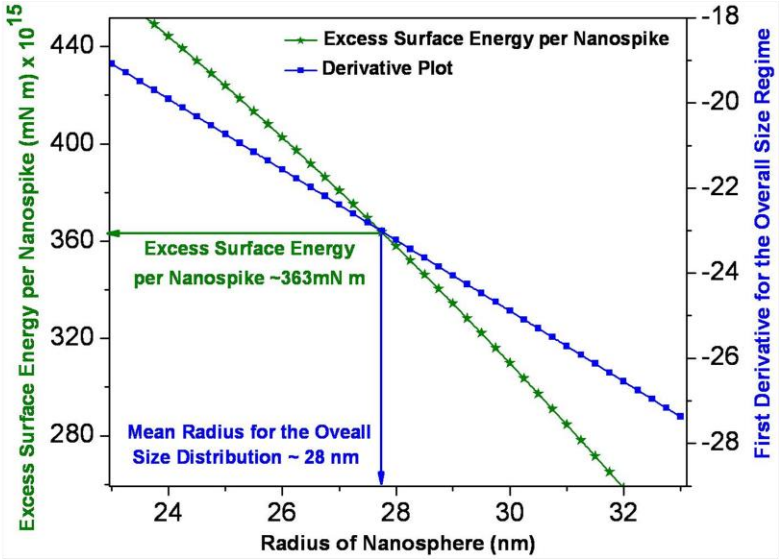

Figure 5.20. Change in excess surface energy of the nanospikes as a function of radius of the evolved nanospheres.

Assuming the surface tension at the gold-water interface as ~33 mN m^{-1},[69] the surface energy per nanostructure of the nanosphere and nanospike is 3.25×10^{-13} and 6.83×10^{-13} mN m, respectively. Thus, the excess surface energy is *ca.* 2.1 times per nanostructure and as the overall surface are is 1.2 fold higher for nanospike campared to nanospheres, the excess surface energy is 2.5 fold higher for the nanospikes than the nanospheres. Therefore, the five-fold quenching efficiency of the molecular probes near the nanospikes is contributed 2.5- and 2.0- fold from the electron and energy transfer mechanism respectively. The theoretical modeling of the nanospikes could act as supplementary to the experimental observation and validates the applicability of the model proposed based on basic Euclidean geometry to calculate the excess surface energy of the anisotropic nanostructures.

5.2.4. Conclusion

In conclusion, this investigation demonstrates that fluorescence quenching of molecular probes near the anisotropic nanostructures does not scale linearly with the surface area; excess surface energy in specific region of the non-spherical particles play a deterministic role in governing the photophysical properties of the molecular probes. This observation has been rationalized by melting experiments while the branched nanostructures have essentially transformed into spherical nanoparticles since sharp tips interact more intensely with NIR laser excitation and probe their role in the modification of the emission characteristics of the dye molecules. The modeling of the tips of the nanospikes based on basic Euclidean geometry and good agreement with the experimentally observed results validates the applicability of the proposed model to calculate the excess surface energy arising from the intriguing anisotropicity of the materials at the nanoscale dimension. The calculation of excess surface energy of the nanospikes as modeled nanostructures could, thus, be envisioned as potentially seeding to a new paradigm in high throughput investigation of the anisotropic nanostructures.

5.3. References

(1) Geddes, C. D. In Metal-Enhanced Fluorescence, John Wiley & Sons, Inc. 2010.

(2) Agranovich, V. M.; Gartstein, Y. N.; Litinskaya, M. *Chem. Rev.* **2011**, *111*, 5179─5214.

(3) Kamat, P. V. *J. Phys. Chem. B* **2002**, *106*, 7729─7744.

(4) Zhao, J.; Zhang, X.; Yonzon, C. R.; Haes, A. J.; Van Duyne, R. P.; Nanomedicine **2006**, *1*, 219─228.

(5) Ghosh, S. K.; Pal, T. *Chem. Rev.* **2007**, *107*, 4797─4862.

(6) Jin, R.; Cao, Y. C.; Hao, E.; Métraux, G .S.; Schatz, G. C.; Mirkin, C. A. *Nature* **2003**, *425*, 487─490.

(7) Huang, X.; Neretina, S.; El-Sayed, M. A. *Adv. Mater*. **2009**, *21*, 4880─4910.

(8) Giannini, V.; Fernández-Domínguez, A. I.; Heck, S. C.; Maier, S. A. *Chem. Rev.* **2011**, *111*, 3888─3912.

(9) Ghosh, S. K.; Pal, T. *Phys. Chem. Chem. Phys.* **2009**, *11*, 3831─3844.

(10) Duan, J.; Nepal, D.; Park, K.; Haley, J. E.; Vella, J. H.; Urbas, A. M.; Vaia, R. A.; Pachter, R. *J. Phys. Chem. C* **2011**, *115*, 13961─13967.

(11) Ming, T.; Zhao, L.; Chen, H.; Woo, K. C.; Wang, J.; Lin, H. -Q. *Nano Lett.* **2011**, *11*, 2296─2303.

(12) Bardhan, R.; Grady, N. K.; Cole, J. R.; Joshi, A.; Halas, N. J. *ACS Nano* **2009**, *3*, 744─752.

(13) Ni, W.; Ambjörnsson, T.; Apell, S. P.; Chen, H.; Wang, J. *Nano Lett.* **2010**, *10*, 77─84.

(14) Fu, Y.; Zhang, J.; Lakowicz, J. R. *J. Am. Chem. Soc.* **2010**, *132*, 5540─5541.

(15) Lu, G.; Zhang, T.; Li, W.; Hou, L.; Liu, J.; Gong, Q. *J. Phys. Chem. C* **2011**, *115*, 15822─15828.

(16) Ming, T.; Zhao, L.; Yang, Z.; Chen, H.; Sun, L.; Wang, J.; Yan, C. *Nano Lett.* **2009**, *9*, 3896─3903.

(17) Tian, L.; Chen, E.; Gandra, N.; Abbas, A.; Singamaneni, S. *Langmuir* **2012**, *28*, 17435─17442.

(18) Lu, X.; Dong, X.; Zhang, K.; Han, X.; Fang, X.; Zhang, Y. *Analyst* **2013**, *138*, 642─650.

(19) Gou, L.; Murphy, C. J.; *Chem. Mater.* **2005**, *17*, 3668─3672.

(20) Brundrett, M. C.; Kendrick, B.; Peterson, C. A. *Histochem.* **1991**, *66*, 111─116.

(21) Yu, H.; Qi, L. *Langmuir* **2009**, *25*, 6781─6786.

(22) Gans, R. *Ann. Phys.* **1912**, *37*, 881─900.

(23) Perez-Juste, J.; Pastoriza-Santos, I.; Liz-Marźan, L. M.; Mulvaney, P. *Coord. Chem. Rev.* **2005**, *249*, 1870─1901.

(24) Novotny, L.; Hecht, B. In *Principles of Nano-Optics*; Cambridge University Press: New York, 2006.

(25) Weitz, D. A.; Garoff, S.; Gersten, J. I.; Nitzan, A. *J. Chem. Phys.* **1983**, *78*, 5324─5338.

(26) Ghosh, S. K.; Pal, A.; Kundu, S.; Nath, S.; Pal, T. *Chem. Phys. Lett.* **2004**, *395*, 366─ 372.

(27) Willets, K. A.; Van Duyne, R. P. *Annu. Rev. Phys. Chem.* **2007**, *58*, 267─297.

(28) Nikoobakht, B.; El-Sayed, M. A. *Langmuir* **2001**, *17*, 6368─6374.

(29) Gao, J. X.; Bender, C. M.; Murphy, C. J. *Langmuir* **2003**, *19*, 9065–9070

(30) El-Khoury, J.M.; Zhou, X.; Qu, L.; Dai, L.; Urbasc, A.; Li, Q. *Chem. Commun*. **2009**, 2109─2111.

(31) Templeton, A. C.; Pietron, J. J.; Murray, R. W.; Mulvaney, P. *J. Phys. Chem. B* **2000**, *104*, 564─570.

(32) Orendorff, C. J.; Alam, T. M.; Sasaki, D. Y.; Bunker, B. C.; Voigt, J. A. *ACS Nano* **2009**, *3*, 971─83.

(33) Benesi, H. A.; Hildebrand, J. H. *J. Am. Chem. Soc*. **1949**, *71*, 2703─2707.

(34) Förster, T. *Ann. Phys.* **1948**, *437*, 55─75.

(35) Waldeck, D. H.; Alivisatos, A. P.; Harris, C. B. *Surf. Sci.* **1985**, *158*, 103─125.

(36) Dulkeith, E.; Morteani, A. C.; Niedereichholz, T.; Klar, T. A.; Feldmann, J.; Levi, S. A.; van Veggel, F. C. J. M.; Reinhoudt, D. N.; Moller, M.; Gittins, D. I. *Phys. Rev. Lett.* **2002**, *89*, 203002 1─4.

(37) Boyen, H. –G.; Ziemann, P.; Wiedwald, U.; Ivanova, V.; Kolb, D. M.; Sakong, S.; Gross, A.; Romanyuk, A.; Büttner, M.; Oelhafen, P. *Nature Mater* **2006**, *5*, 394─399.

(38) Lakowicz, J. R. In *Principles of Fluorescence Spectroscopy*, 3rd Ed., Plenum Press, New York, 2006.

(39) De, S.; Pal, A.; Jana, N. R.; Pal, T. *J. Photochem. Photobiol. A* **2000**, *131*, 111─123.

(40) Quyang, G.; Wang, C. X.; Yang, G. W. *Chem. Rev*. **2009**, *109*, 4221─4247.

(41) Maier, S. A. In *Plasmonics: Fundamentals and Applications* 2007, Springer-Verlag, USA.

(42) Burda, C.; Chen, X. B.; Narayanan, R.; El-Sayed, M. A. *Chem. Rev.* **2005**, *105*, 1025─1102.

(43) Grzelczak, M.; Pérez-Juste, J.; Mulvaney, P.;Liz-Marzán, L. M. *Chem. Soc. Rev.* **2008**, *37*, 1783─1791.

(44) Stewart, M. E.; Anderton, C. R.; Thompson, L.B.; Maria, J.; Gray, S. K.; Rogers, J. A.; Nuzzo, R. G. *Chem. Rev.* **2008**, *108*, 494─521.

(45) Alvarez, M. M.; Khoury, J. T.; Schaaff, T. G.; Shafigullin, M. N.; Vezmar, I.; Whetten, R. L. *J. Phys. Chem. B* **1997**, *101*, 3706─3712.

(46) Alvarez-Puebla, R.; Liz-Marzán, L. M.; F. de Abajo, J. G. *J. Phys. Chem. Lett.* **2010**, *1*, 2428─2434.

(47) Hao, E.; Bailey, R. C.; Schatz, G. C.; Hupp, J. T.; Li, S. *Nano Lett.* **2004**, *4*, 327─330.

(48) Hao, F.; Nehl, C. L.; Hafner, J. H.; Nordlander, P. *Nano Lett.* **2007**, *7*, 729─732.

(49) Ozbay, E. *Science* **2006**, *311*, 189−193.

(50) Thomas, K. G.; Kamat, P. V. *Acc. Chem. Res.* **2003**, *36*, 888–898.

(51) Gurkov, T. D.; Kralchevsky, P. A. *Colloids Surf.* **1990**, *41*, 45–68.

(52) Jana, N. R.; Gearheart, L.; Murphy, C. J. *Adv. Mater.* **2001**, *13*, 1389–1393.

(53) Sau, T. K.; Rogach, A. L.; Döblinger, M.; Feldmann, J. *Small* **2011**, *7*, 2188–2194.

(54) Claro, A.; Melo, M. J.;Schäfer, S.; de Melo, J. S. S.; Pina, F.; van den Berg, K. J.; Burnstock, A. *Talanta* **2008**, *74*, 922–929.

(55) Miliani, C.; Romani, A.; Favaro, G. *J. Phys. Org. Chem.* **2000**, *13*, 141–150.

(56) Prodan, E.; Radloff, C.; Halas, N. J.; Nordlander, P. *Science* **2003**, *302*, 419–422.

(57) Otto, S.; Volmer, M. *Phys. Z.* **1919**, *20*, 183–188.

(58) Makarova, O. V.; Ostafin, A. E.; Miyoshi Jr., H.; Norris, J. R.; Miesel, D. *J. Phys. Chem. B* **1999**, *103*, 9080–9084.

(59) Förster, T. *Ann. Phys.* **1948**, *437*, 55−75.

(60) Fan, C.; Wang, S.; Hong, J. W.; Bazan, G. C.; Plaxco, K. W.; Heeger, A. *Proc. Natl. Acad. Sci.* **2003**, *100*, 6297–6301.

(61) Smart, L. E.; Moore, E. A. In *Solid State Chemistry: An Introduction* 3rd edn., Taylor & Francis, CRC Press: Boca Raton, Florida, USA.

(62) Smith, B. A.; Zhang, J. Z., Giebel, U., Schmid G. *Chem. Phys. Lett.* **1997**, *270*, 139–144.

(63) Mafuné, F., Kohno, J. Y., Takeda, Y., Kondow, T., Schwabe, H. *J. Phys. Chem. B* **2000**, *104*, 8333–8337.

(64) Link, S.; El-Sayed, M. A. *Annu. Rev. Phys. Chem.* **2003**, *54*, 331–366.

(65) Chen, H. M.; Liu, R. –S. *J. Phys. Chem. C* **2011**, *115*, 3513–3527.

(66) Weisstein, E. W. Euclid's Postulates In *CRC Concise Encyclopedia of Mathematics* 2nd edn., 2003, CRC Press, p. 942.

(67) Halsey, G. *J. Chem. Phys.* **1948**, *16*, 931–937.

(68) Menger, F. M.; Rizvi, S. A. A. *Langmuir* **2011**, *27*, 13975–13977.

(69) Nicole, G.; Adams, D. J.; Böker, A.; Krausch, G. *Langmuir* **2006**, *16*, 2539─2547.